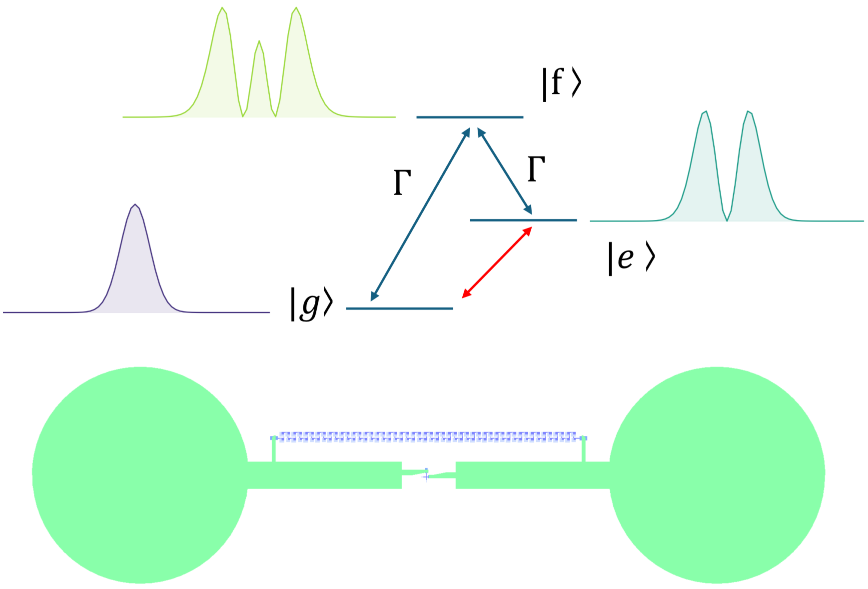

Circuit Waveguide Electrodynamics with Fluxonium Qubits

Engineering dissipation for fluxonium atoms

Erasmus Mundus Master Nanoscience and Nanotechnology

Quantum Computing Track

Saba Kheviashvili

DEPARTMENT OF Microtechnology and Nanoscience

CHALMERS UNIVERSITY OF TECHNOLOGY
Gothenburg, Sweden 2026
www.chalmers.se

Master's thesis 2026

Circuit Waveguide Electrodynamics with Fluxonium Qubits

Engineering dissipation for fluxonium atoms

Saba Kheviashvili

Department of Microtechnology and Nanoscience
Quantum Technology Laboratory (QT)
202Q Lab
Chalmers University of Technology
Gothenburg, Sweden 2026

Circuit Waveguide Electrodynamics with Fluxonium Qubits
Engineering dissipation for fluxonium atoms
Saba Kheviashvili

Supervisor: Aamir Ali, Quantum Technology Laboratory, Chalmers
Examiner: Simone Gasparinetti, Quantum Technology Laboratory, Chalmers
Co-promoter : Kristiaan De Greve, Department of Electrical Engineering, KUL
Referee : Thilo Bauch, Quantum Device Physics Laboratory, Chalmers

Master’s Thesis 2026
Department of Microtechnology and Nanoscience
Quantum Technology Laboratory (QT)
202Q Lab
Chalmers University of Technology
SE-412 96 Gothenburg
Telephone +46 31 772 1000

Typeset in LaTeX
Printed by Chalmers Reproservice
Gothenburg, Sweden 2026

Circuit Waveguide Electrodynamics with Fluxonium Qubits
Engineering dissipation for fluxonium atoms
Saba Kheviashvili
Department of Microtechnology and Nanoscience
Chalmers University of Technology

Abstract

Fluxonium circuits are emerging as a promising alternative to transmons for quantum information processing. In addition to the standard capacitor and Josephson junction, a fluxonium includes a superinductor, which suppresses charge noise, increases coherence, and provides large anharmonicity. Its rich transition spectrum, governed by non-trivial selection rules sensitive to external flux, enables dissipation engineering with potential applications that include fluorescence-based resonator-free readout, electromagnetically induced transparency, and Λ-systems. Previous studies have mostly relied on three-dimensional waveguides or cavities, which limit circuit scalability and integration of elements such as Purcell filters. In this work, we fabricate fluxoniums using Josephson junction arrays as superinductors and couple them to both coplanar-waveguide resonators and semi-infinite transmission-line waveguides for comparative studies. We characterize dispersive coupling to resonators, demonstrating tunability via external flux. Using spectroscopy, we identify transitions among the first four energy levels (0-1, 0-2, 1-2, 0-3) in a fluxonium coupled to a waveguide. We perform power-dependent measurements to extract coupling rates, which are consistent with theoretical predictions. We identify a parameter regime where the 0-1 transition is suppressed while 0-2 and 1-2 remain comparable, providing a pathway to implement a Λ-system within a single artificial atom. Future device iterations aim to optimize this regime, with the ultimate goal of realizing a robust single-atom microwave photodetector.

Keywords: quantum technology, qubit, fluxonium, cQED, dissipation engineering, Lindblad master equation, waveguide electrodynamics

Acknowledgements

I would like to express my sincere gratitude to my examiner, Simone Gasparinetti, for the opportunity to work on this project and for invaluable support and insight. I am deeply grateful to my supervisor, Aamir Ali, for guidance, patience, and encouragement throughout my master's thesis. I also thank Thomas Descamps for fabricating the sample used in our experiments, and everyone in the 202Q lab for their assistance. The fluxonium design used in this thesis was inspired by work from Professor Christian Andersen's lab at TU Delft; I thank Professor Andersen and his PhD student Figen Yilmaz for assistance with the design and simulations, and Lukas Splitthoff for supporting the design and fabrication efforts. Finally, my heartfelt thanks go to my family and friends for their unwavering support. To my grandpa.

Saba Kheviashvili, Gothenburg, August 2025

List of Acronyms

Below is the list of acronyms that have been used throughout this thesis listed in alphabetical order:

cQED	Circuit Quantum Electrodynamics
COMSOL	COMSOL Multiphysics (finite-element solver)
CPW	Coplanar Waveguide
CW	Continuous Wave
DC	Direct Current
EPR	Energy Participation Ratio
GDS	Graphic Data System (layout file format)
HEMT	High Electron-Mobility Transistor
HFSS	(Ansys) High-Frequency Structure Simulator
IF	Intermediate Frequency
IQ	In-phase/Quadrature
JJ	Josephson Junction
JJA	Josephson-Junction Array (superinductor)
LO	Local Oscillator
MXC	Mixing Chamber (base stage of dilution fridge)
RF	Radio Frequency (microwave)
VNA	Vector Network Analyzer

Nomenclature

Below is the nomenclature of indices, sets, parameters, and variables that have been used throughout this thesis.

Φ_0	Magnetic flux quantum ($h/2e$)
Φ_{ext}	External magnetic flux threading the loop
ϕ	Reduced flux / superconducting phase across the junction
E_J	Josephson energy
E_C	Charging energy
E_L	Inductive energy (from superinductance)
L_J	Josephson inductance
C_J	Junction capacitance
L_s	Superinductance
$\lvert i\rangle$	Fluxonium eigenstate with level index i
ω_{ij}, f_{ij}	Angular frequency / frequency of the $i \leftrightarrow j$ transition
g	Atom–resonator coupling rate
κ_c	Resonator coupling (external) decay rate
κ_i	Resonator internal loss rate
$\kappa = \kappa_c + \kappa_i$	Total resonator linewidth
Q_c, Q_i, Q_ℓ	Coupling, internal, and loaded quality factors
Γ_r	Radiative decay rate of a transition
Γ_{nr}	Non-radiative decay rate
$\Gamma = \Gamma_r + \Gamma_{nr}$	Total decay rate
S_{21}	Forward transmission coefficient (VNA)
S_{11}	Reflection coefficient (VNA)
P_{in}	Input power at the device plane
I_Φ	Flux-line bias current
$I_{1/2\Phi_0}$	Bias current for half a flux quantum in the loop
Δ	Detuning between drive and transition frequency

Z_0	Line characteristic impedance (typically 50 Ω)
T	Temperature (e.g., MXC stage)
$\hbar$	Reduced Planck's constant ($h/2\pi$)
Λ	Three-level Λ-system

Indices

i, j	Indices for fluxonium energy levels
n	Photon (Fock) number index
t	Time/sample index in acquisitions
k	Electromagnetic mode index
b	Bias point (flux/current) index
r	Repetition/average index

Contents

List of Figures

List of Tables

1

Introduction

Quantum theory explains nature at microscopic scales where classical physics fails. It describes everything with quantum state vectors that live in a Hilbert space and explains phenomena such as entanglement and superposition. Over the past few decades, these concepts converged into engineered quantum platforms that allow us to design experiments on single quantum systems and their coherent manipulation[3]. This set the stage for quantum technologies implemented with light-matter interactions arising in superconducting electrical circuits.

Quantized electromagnetic fields interacting with two-level systems is the study of cavity or circuit quantum electrodynamics (QED). In circuit QED, light interacts with artificial atoms that are made by replacing an oscillator in an LC circuit with a Josephson junction (JJ). With high level of impedance control, engineering coupling to exceed dissipation rates has been achieved, which is called a strong coupling regime.

A superconducting artificial atom is an electrical circuit containing one or more JJs that yields an anharmonic spectrum. The energy scale is set by energy scales: Josephson energy E_J, charging energy E_C, and – for fluxonium – inductive energy E_L. There is a tradeoff between anharmonicity, coherence, and ease of control when choosing these energy scales. The artificial atoms in cQED offer a promising platform for quantum computation because their properties, such as resonance frequency and coupling, can be designed and tuned, even in-situ.

Even though it is critical to isolate a quantum system so that it maintains coherence, carefully *engineered* dissipation can be useful in quantum technology, for example for stabilizing desired states and accelerating qubit reset. In the picture of open quantum systems (often called Lindblad picture, see Fig. 1.1), coupling selected transitions to baths with tailored rates implements desired quantum state preparation, stabilization of cat states, and rapid qubit initialization [4, 5, 6]. In circuit QED, this is realized for example by impedance-matched environments, engineered Purcell filters, etc. For fluxonium, dissipation engineering can be achieved as simply as changing the external flux threaded in the loop, as it changes the transition matrix elements, effectively changing coupling to the environment. This is especially powerful because coupling to the environment can be tuned even in-situ.

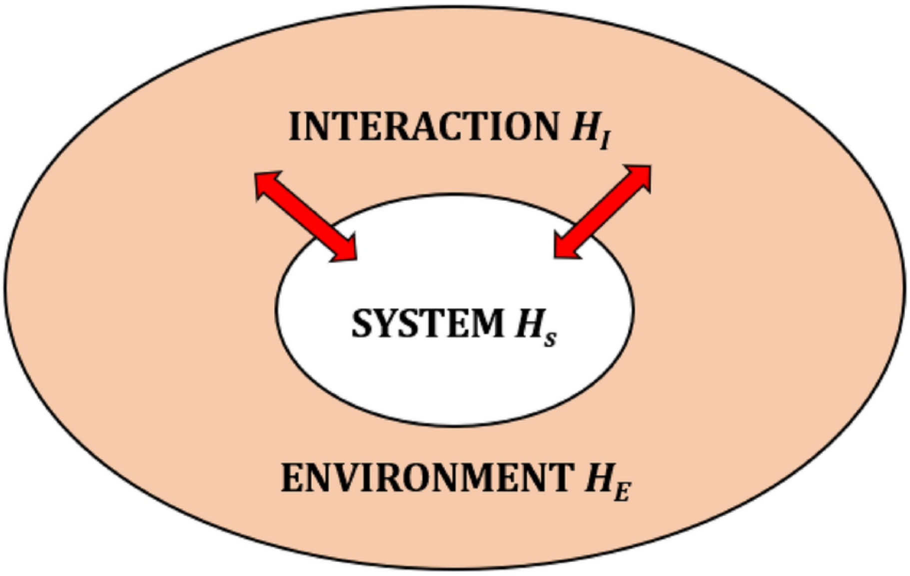

Figure 1.1: Schematic of a quantum system interacting with the environment.

Superconducting fluxonium atoms offer increased anharmonicity, increased coherence and flux-tunable selection rules that make them ideal for engineering dissipation of multilevel atoms. The fluxonium Hamiltonian,

$$H = 4E_C n^2 + \frac{1}{2}E_L(\phi - \phi_{\text{ext}})^2 - E_J \cos\phi,$$

captures the interplay of three different energy scales: charging, inductive and Josephson, while also accounting for external flux. In the regime when $E_L \ll E_J$ and external flux equals half flux quantum the potential forms two wells whose lowest two states constitute the qubit, and this point has been widely used in quantum computation. However, fluxonium is also appealing for engineering dissipative rates which is why very recently fluxonium directly coupled to a waveguide was used for quantum-nondemolition (QND) fluorescence readout [7].

This thesis asks a main question: can we engineer an artificial fluxonium atom and its electromagnetic environment to selectively enhance or suppress transitions that will realize a Λ system? We address this question by designing, simulating and measuring the fabricated devices coupled to planar readout resonators or coplanar waveguide baths.
The remainder of this thesis is organized as follows:

- **Chapter 2 (Theory):** Circuit-QED foundations and fluxonium theory, including waveguide coupling and the input-output model used later for rate extraction. This chapter also introduces the selection-rule picture that motivates Λ-engineering.
- **Chapter 3 (Methods):** Design (junction choices, array superinductor), HFSS + EPR simulation flow, and cryogenic wiring/measurement techniques.
- **Chapter 4 (Results):** (A,B) Resonator devices: punch-out and flux-dispersive checks of functionality; (C) Waveguide device: mapping 0–1/0–2/1–2/0–3 transitions versus flux, quantitative Γ_{r} and Γ_{nr} fits, and identification of a Λ-friendly flux region.

- **Chapter 5 (Conclusion):** Summarizing the main results in the thesis; Outlook and next steps.

2

Theory

This section gives a theoretical background to introduce fluxoniums. We start with introducing circuit quantum electrodynamics (cQED) with waveguides, general circuit quantization and artificial atoms in cQED. Then we proceed with fluxoniums, discuss its characteristics and explain how we can characterize the interaction with the environment.

2.1 Circuit quantum electrodynamics

Circuit quantum electrodynamics (cQED) studies the interaction between superconducting artificial atoms and their environment, particularly the electromagnetic radiation confined in a cavity [8]. These systems operate in the microwave domain and are inspired by cavity quantum electrodynamics (CQED), which studies excitations that are coherently exchanged between real atoms and quantized electromagnetic fields inside optical or microwave cavities [9].

In order to observe coherent interactions, the atom–cavity coupling strength must exceed the individual decay rates of both the atom and the cavity. This strong coupling regime was first achieved in a circuit QED system in 2004 [10]. Since then, circuit QED has emerged as a leading platform for building quantum computers and for exploring a wide range of quantum phenomena. Compared to cavity QED, circuit QED offers several key advantages: greater tunability (even in situ), stronger light–matter coupling, and superior scalability [11].

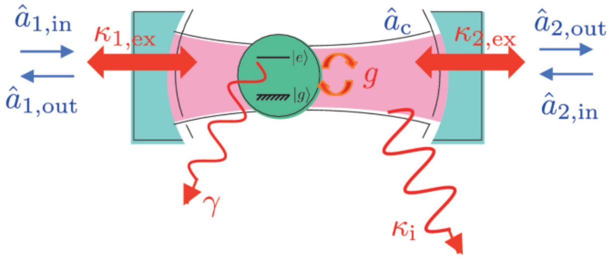

Figure 2.1: Basic architecture in cavity and circuit QED: atom coupled to the cavity

2.1.1 Circuit Quantization

The natural way to introduce circuit quantization is to first start with a classical counterpart - LC circuit. We model it as a lumped element circuit [12]. This is valid as EM fields used in cQED experiments are of GHz frequencies, corresponding to wavelengths $\lambda \sim 10$mm, and largest components used in the circuits have dimensions $a \sim 100\mu$m, satisfying $\lambda \gg a$. A capacitor is described as an element satisfying $q = CV$. It is in series with an inductor with a relation $\Phi = LI$. We can define a flux variable ϕ which is just a time integral of voltage:

$$\phi = \int_{-\infty}^{t} V(t)dt \tag{2.1}$$

The energy stored in the capacitor is

$$E_c = \frac{1}{2}C\dot{\phi}^2 \tag{2.2}$$

On the other hand, energy in the inductor with inductance L is

$$E_l = \frac{1}{2L}\phi^2 \tag{2.3}$$

Following the treatment in classical mechanics [13], we define the Lagrangian:

$$L(\phi, \dot{\phi}, t) = \frac{1}{2}C\dot{\phi}^2 - \frac{1}{2L}\phi^2 \tag{2.4}$$

Where the variable ϕ plays the role of the coordinate. Accordingly, we can think of capacitance C as a mass, and of $\frac{1}{L}$ as a spring constant.

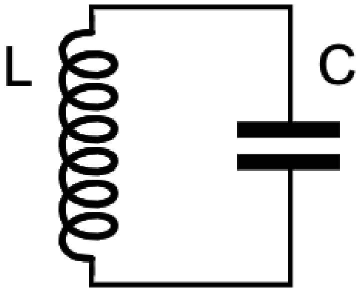

Figure 2.2: LC Lumped Element circuit comprised of an inductor and a capacitor

The conjugate variable to flux ϕ is found as usual:

$$\frac{\partial L}{\partial \dot{\phi}} = C\dot{\phi} = q \tag{2.5}$$

which is just the excess charge on the capacitor.

$$H(\phi, q, t) = \dot{\phi}q - L(\phi, \dot{\phi}, t) = \frac{1}{2C}q^2 + \frac{1}{2L}\phi^2 \tag{2.6}$$

Hamilton's equations of motion read

$$\dot{\phi} = \frac{\partial H}{\partial q} = \frac{q}{C}, \qquad \dot{q} = -\frac{\partial H}{\partial \phi} = -\frac{\phi}{L} \tag{2.7}$$

To quantize the modes, we promote classical variables ϕ and q to quantum variables $\hat{\phi}$ and $\hat{q}$ obeying commutation relation

$$[\hat{\phi}, \hat{q}] = i\hbar \tag{2.8}$$

The Hamiltonian becomes an operator:

$$\hat{H} = \frac{1}{2C}\hat{q}^2 + \frac{1}{2L}\hat{\phi}^2. \tag{2.9}$$

We now introduce dimensionless annihilation and creation operators $\hat{a}$ and $\hat{a}^\dagger$ via:

$$\hat{\phi} = \phi_{\text{zpf}}(\hat{a} + \hat{a}^\dagger), \tag{2.10}$$

$$\hat{q} = -iq_{\text{zpf}}(\hat{a} - \hat{a}^\dagger), \tag{2.11}$$

where the zero-point fluctuation amplitudes are defined as

$$\phi_{\text{zpf}} = \sqrt{\frac{\hbar Z}{2}}, \qquad q_{\text{zpf}} = \sqrt{\frac{\hbar}{2Z}}, \tag{2.12}$$

and $Z = \sqrt{L/C}$ is the characteristic impedance of the LC oscillator.
Substituting into the Hamiltonian gives

$$\hat{H} = \hbar\omega\left(\hat{a}^\dagger\hat{a} + \frac{1}{2}\right), \tag{2.13}$$

with the oscillator frequency

$$\omega = 1/\sqrt{LC} \tag{2.14}$$

This is the standard quantum harmonic oscillator spectrum, where energy levels are equally spaced by $\hbar\omega$.
In the quantum ground state $|0\rangle$, the expectation values of $\hat{\phi}$ and $\hat{q}$ vanish, but their variances do not. These fluctuations are known as zero-point fluctuations:

$$\langle 0|\hat{\phi}^2|0\rangle = \phi_{\text{zpf}}^2 = \frac{\hbar Z}{2}, \tag{2.15}$$

$$\langle 0|\hat{q}^2|0\rangle = q_{\text{zpf}}^2 = \frac{\hbar}{2Z}. \tag{2.16}$$

It is useful to think of them as voltage and current vacuum fluctuations, because voltage is just

$$\hat{V} = \frac{\hat{Q}}{C} = -\frac{1}{C}iq_{\text{zpf}}(\hat{a} - \hat{a}^\dagger) = -iV_{zpf}(\hat{a} - \hat{a}^\dagger) \tag{2.17}$$

where we used

$$V_{zpf} = \sqrt{\frac{\hbar\omega}{2C}} \tag{2.18}$$

It is useful to express the zero-point fluctuations in terms of the resistance quantum

$$R_Q = \frac{\hbar}{(2e)^2} \approx 6.45\,\mathrm{k}\Omega, \tag{2.19}$$

which naturally appears when working with superconducting circuits and Josephson junctions. We will also see it while discussing the Josephson junction array of fluxonium.

We can define the dimensionless impedance ratio $r = Z/R_Q$, which allows us to express the ZPF amplitudes as

$$\phi_{\mathrm{zpf}} = \sqrt{\frac{\hbar Z}{2}} = \frac{\hbar}{2e}\sqrt{\frac{r}{2}}, q_{\mathrm{zpf}} = \sqrt{\frac{\hbar}{2Z}} = 2e\sqrt{\frac{1}{2r}}. \tag{2.20}$$

These expressions highlight the duality between charge and flux: circuits with large impedance (e.g., superinductors [14]) exhibit large flux fluctuations and small charge fluctuations, while low-impedance circuits (e.g., transmons[15]) do the opposite. This balance plays a central role in the design of superconducting qubits.

Before quantising a lumped–element circuit we must check that the system is indeed able to resolve its discrete quantum levels. Two inequalities guarantee this [16, 11]:

$$\boxed{\underbrace{\kappa}_{\text{linewidth}} \quad \ll \quad \underbrace{\omega_0}_{\text{level spacing}} \qquad \Longleftrightarrow \qquad Q \equiv \frac{\omega_0}{\kappa} \gg 1} \tag{2.21}$$

$$\boxed{k_{\mathrm{B}}T \;\ll\; \hbar\omega_0} \tag{2.22}$$

Equation (2.21) demands a high quality factor; superconducting metals are therefore employed to suppress Ohmic loss and reach $Q \sim 10^{5\text{–}7}$ in planar resonators. Equation (2.22) requires dilution–refrigerator temperatures ($T \lesssim 20$ mK so that $k_{\mathrm{B}}T/h \approx 0.4$ GHz $\ll \omega_0/2\pi$ for qubit frequencies in the 4–8 GHz band).

As we are using superconducting metal, namely Aluminum in our experiments, we have some additional spectral safety margins. The bulk plasma frequency of aluminium is $\hbar\omega_p \approx 15$ eV ($\omega_p/2\pi \approx 3.6$ PHz) [17]. Because our microwave drive satisfies $\omega_0 \ll \omega_p$, plasmon modes are pushed far out of the spectrum and can therefore be neglected.

Cooper-pair breaking sets in when $\hbar\omega$ exceeds the gap energy $2\Delta_{\mathrm{Al}} \simeq 3.4 \times 10^{-4}$ eV, which corresponds to a threshold frequency [18, 17]

$$f_{\mathrm{gap}} = \frac{2\Delta_{\mathrm{Al}}}{h} \approx 8.2 \times 10^{10}\ \mathrm{Hz}\ (82\ \mathrm{GHz}). \tag{2.23}$$

Operating in the GHz range ($\omega_0 \ll 2\Delta_{\mathrm{Al}}/\hbar$) keeps Cooper pairs intact and suppresses quasiparticle-induced dissipation.

Taken together, inequalities (2.21)–(2.22) and the two spectral cut-offs above define a safe window in which lumped superconducting circuits behave as clean, low-loss oscillators that can be quantised. We can now assign a clear physical interpretation to the modes of the electrical quantum harmonic oscillator: they correspond to the dissipationless flow of Cooper-pair current between the capacitor plates at the discrete frequencies $n\omega$, where the fundamental frequency ω is defined in Eq. (2.14)[19].

2.1.2 Josephson junction non-Linearity

Quantum LC oscillators, like their mechanical analogs, have equidistant energy spectra. In order to be able to discriminate energy levels, we would need to add some kind of nonlinearity to the system. Circuit-QED solves this by inserting a *Josephson junction*—a dissipation-free but strongly *non-linear* inductor whose dynamics obey the *dc* and *ac* Josephson relations [20]:

$$I_s(t) = I_c \sin\phi(t), \tag{2.24}$$

$$V(t) = \frac{\hbar}{2e}\,\dot{\phi}(t) = \frac{\Phi_0}{2\pi}\,\dot{\phi}(t), \qquad \Phi_0 \equiv \frac{h}{2e} \approx 2.07 \times 10^{-15}\,\mathrm{Wb}, \tag{2.25}$$

where I_c is the critical current and ϕ the condensate phase drop across the tunnel barrier. Because I_s depends *sinusoidally* on ϕ while $V \propto \dot{\phi}$, even a single junction breaks the harmonic ladder.
Starting from (2.24) take its time derivative:

$$\dot{I}_s(t) = I_c \cos\phi(t)\,\dot{\phi}(t). \tag{2.26}$$

Define an *instantaneous* inductance $L_J(\phi)$ through the usual inductor rule $V = L_J\,\dot{I}_s$. Eliminating $\dot{\phi}$ gives

$$\frac{\Phi_0}{2\pi}\,\dot{\phi} \;=\; L_J(\phi)\,I_c\cos\phi\,\dot{\phi} \quad\Longrightarrow\quad \boxed{L_J(\phi) = \frac{\Phi_0}{2\pi\,I_c\cos\phi}} \tag{2.27}$$

Hence the Josephson inductance is strongly *non-linear*, diverging at $\phi = \pm\pi/2$ and reducing, for small oscillations, to

$$L_{J0} = L_J(\phi{=}0) = \frac{\Phi_0}{2\pi I_c}. \tag{2.28}$$

We can derive energy stored in such an inductor following way :
Any lumped element obeys

$$U(t) \;=\; \int_0^t v(t')\,i(t')\,\mathrm{d}t', \tag{2.29}$$

where v is the voltage across the element and i the current through it. Inserting the equations (2.24) and (2.25):

$$\begin{aligned} U_J &= \int v\,i\,dt = \int I_c\sin\phi\,\frac{\Phi_0}{2\pi}\,\dot{\phi}\,dt = \frac{\Phi_0 I_c}{2\pi}\int \sin\phi\,d\phi \\ &= \frac{\Phi_0 I_c}{2\pi}\Big(1-\cos\phi\Big) \;=\; E_J\Big(1-\cos\phi\Big), \end{aligned} \tag{2.30}$$

where $E_J \equiv \Phi_0 I_c/2\pi$ is the *Josephson energy*. Up to an irrelevant constant, the Josephson potential is therefore

$$U_J(\phi) \;=\; -E_J\cos\phi. \tag{2.31}$$

2.1.3 Coplanar waveguide transmission-line modes

Waveguides channel EM fields along a specified axis by means of boundary conditions. In planar superconducting chips, the most widely used geometry is coplanar waveguides [21], where a centre conductor of width w is separated from two ground planes by s, both of thickness t. This geometry supports a quasi-TEM mode, where the electromagnetic fields are mostly contained between the gap of the center conductor and two ground planes. In our experiments, Aluminum is used as a conductor, which is deposited on Silicon.

If we cool down this structure below the critical temperature for superconductivity ($\approx$ 1.2K for Aluminum), we essentially get lossless propagation of EM fields along the waveguide [11]. We can model this geometry by lumped-element analog, with per-unit-length capacitance C' and inductance L'. Line's characteristic impedance and propagation speed become[22]:

$$Z_0 = \sqrt{\frac{L'}{C'}} \qquad v_p = \frac{1}{\sqrt{L'C'}} \tag{2.32}$$

If the CPW is terminated at only one end, it forms a *semi-infinite transmission line*. Quantizing then yields a continuum of modes, $a_w,\ w \in [0, \infty)$, with a Hamiltonian

$$\hat{H}_{\mathrm{TL}} = \int_0^\infty d\omega\ \hbar\omega\ \hat{a}_\omega^\dagger \hat{a}_\omega \tag{2.33}$$

Any quantum circuit coupled with rate κ obeys the input–output relation

$$a_{\mathrm{out}}(t) = a_{\mathrm{in}}(t) - \sqrt{\kappa}\, b(t), \tag{2.34}$$

so the line acts as an *effective dissipative bath*: although the aluminium CPW itself is virtually loss-free, photons that leak into the continuum never return [19].

If the same aluminium CPW is terminated (shorted or open) at both ends —for it becomes a Fabry–Pérot cavity with standing-wave boundary conditions. For a section of physical length L the resonance frequencies are

$$f_n^{(\lambda/2)} = \frac{(n+1)\, v_{\mathrm{p}}}{2L}, \qquad f_m^{(\lambda/4)} = \frac{(2m+1)\, v_{\mathrm{p}}}{4L}, \qquad n, m \in \mathbb{N}, \tag{2.35}$$

depending on whether each end is open or shorted.

2.2 Fluxonium

The fluxonium artificial atom, introduced in 2009 [23], offers two major advantages over the Cooper-pair box and the transmon: (i) reduced sensitivity to offset charge and (ii) larger intrinsic anharmonicity. The circuit is built by shunting a small Josephson junction ($E_J \sim$ 5–10 GHz) with a superinductor, forming a loop whose transition spectrum can be tuned by an external magnetic flux.

Purely geometric inductors are limited to characteristic impedances below the vacuum impedance $Z_0 = \sqrt{\mu_0/\varepsilon_0} \simeq 377\,\Omega$. To reach the large phase-fluctuation regime $\langle\phi^2\rangle^{1/2} \gtrsim 1$ one instead uses kinetic inductors: a series array of N Josephson junctions, each with $L_J = (\Phi_0/2\pi)^2/E_J$, gives

$$L_{\text{array}} = N L_J,$$

providing hundreds to thousands of nanohenries of inductance without dissipation [24].

With sub-gigahertz level spacing at the sweet spot ($f_{01} \lesssim 1$ GHz) a fluxonium at dilution-refrigerator temperatures naturally sits in the regime $k_B T \sim h f_{01}$: thermal excitations need to be taken into account, for example during the reset, yet at this point coherence times become large. This operating point, combined with strong anharmonicity, makes fluxonium a possibly useful platform for quantum thermodynamics: potential applications in fluorescence-based resonator-free readout, electromagnetically induced transparency, and Λ-systems.

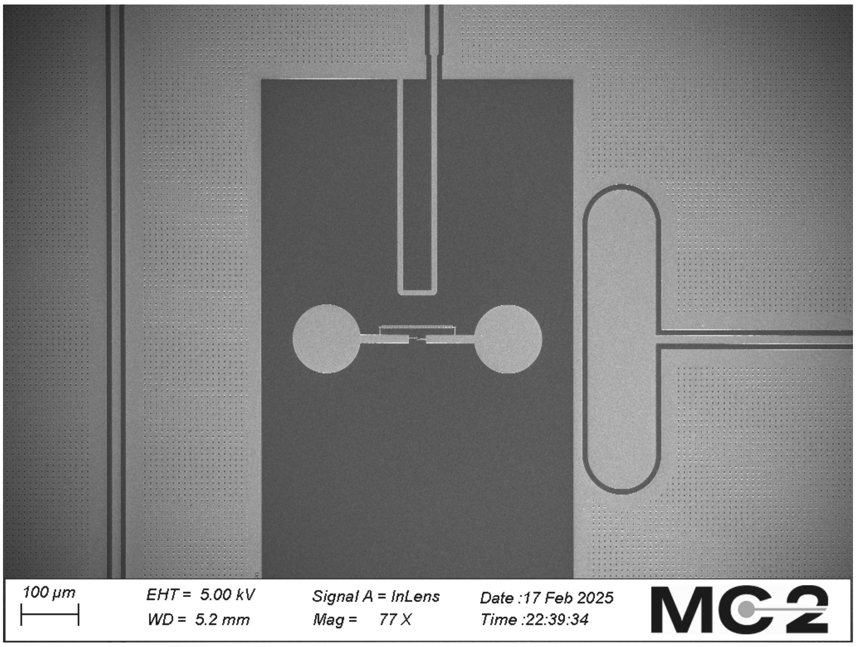

Figure 2.3: Fluxonium device used in this thesis. It comprises of two superconducting pads, connected via single Josephson Junction and Josephson Junction array, flux line and a waveguide.

2.2.1 Circuit topology and Hamiltonian

The fluxonium circuit consists of three lumped elements in parallel:

- a small Josephson junction with Josephson energy E_J,
- a large linear inductance L_{array} provided by a series array of N Josephson junctions,
- a stray shunt capacitance C to ground.

Now let us write down the Lagrangian of the circuit. If we choose flux across the single Josephson junction as an independent variable, the classical Lagrangian of the system will be:

$$\mathcal{L} = \frac{C}{2}\,\dot{\Phi}^2 + E_J \cos\!\left(\frac{2\pi\Phi}{\Phi_0}\right) - \frac{1}{2L_{\text{array}}}\left(\Phi - \Phi_{\text{ext}}\right)^2. \tag{2.36}$$

Then let us promote the classical variables to quantum, and introduce the reduced form, $\hat{n} = \hat{Q}/2e$, $\hat{\phi} = 2\pi\hat{\Phi}/\Phi_0$, $\phi_{\text{ext}} = 2\pi\Phi_{\text{ext}}/\Phi_0$. Now the Hamiltonian reads:

$$\boxed{\hat{H} = 4E_C\,\hat{n}^2 - E_J\cos(\hat{\phi} - \phi_{\text{ext}}) + \frac{1}{2}E_L\hat{\phi}^2} \tag{2.37}$$

2.2.2 Energy spectrum and eigenstates

The fluxonium Hamiltonian gives rise to two different sets of excitations - plasmons and fluxons. Numerical diagonalization in the coordinate (flux) basis $\left\langle\phi\middle|\psi_k\right\rangle$ yields the spectrum. Now we can analyze this spectrum for different parameters. The three energy scales and external flux play different roles.

Changing the Josephson energy E_J changes, as expected, the nonlinearity of the system. If E_J is small, the circuit is to a good approximation an LC oscillator; therefore, increasing E_J also increases the anharmonicity. At half a flux quantum ($\Phi_{\text{ext}} = \Phi_0/2$), we see that E_J sets the height of the barrier between the two wells.

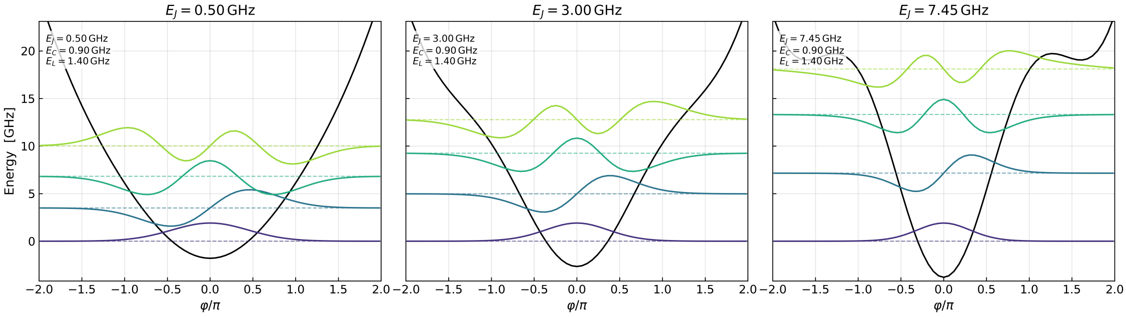

(a) Changing E_j while fixing other parameters at zero external flux. Solid black: potential $U(\phi)$. Colored solid/dashed: energy and wavefunctions (respectively) of the first four states.

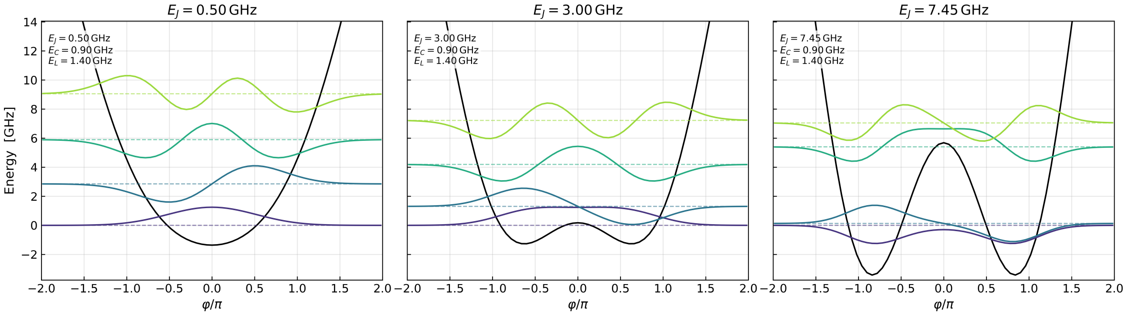

(b) Changing E_J while fixing other parameters at half a flux quantum.

We can also see how changing E_L affects the spectrum. Increasing it makes the spectrum more harmonic. That is why usually fluxoniums operate in the $E_J/E_L \gg 1$ regime, which makes the circuit more anharmonic. Therefore, the ratio E_J/E_L determines the system's harmonicity.

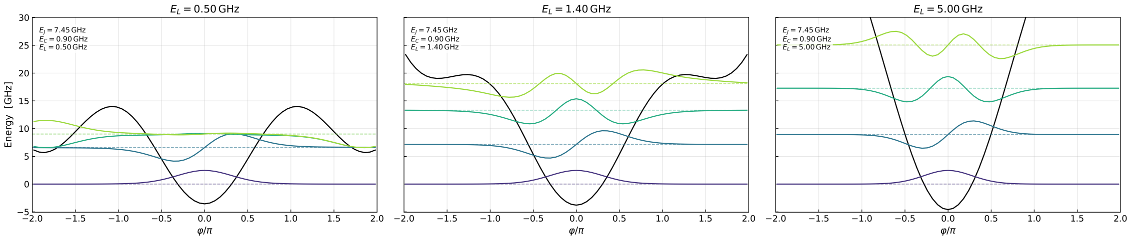

(a) Changing E_L while fixing other parameters at zero external flux.

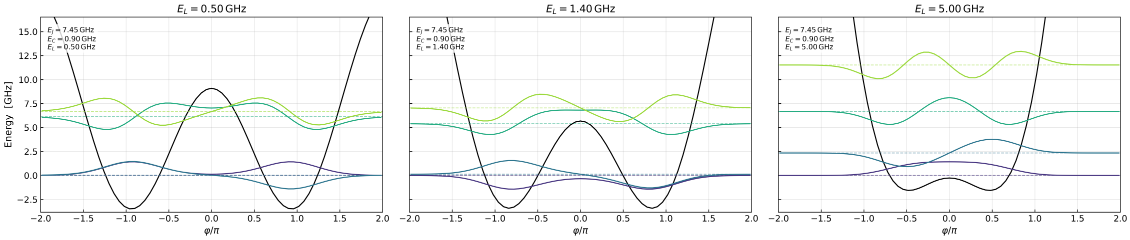

(b) Changing E_L while fixing other parameters at half a flux quantum.

E_C sets the overall energy scale of the system. Small E_C suppresses charge noise and is typical for heavy-fluxonium designs used in long-coherence experiments [25]. High E_C together with moderate E_J yields the light-fluxonium regime, useful for fast, strong-drive control. The ratio of E_J/E_C determines the ω_{01} transition frequency at half flux, as tunneling between wells depends exponentially on it [26].

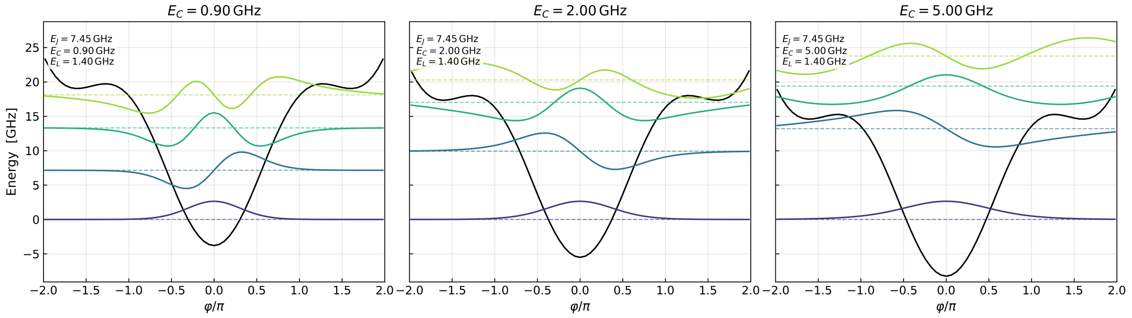

(a) Changing E_C while fixing other parameters at zero external flux.

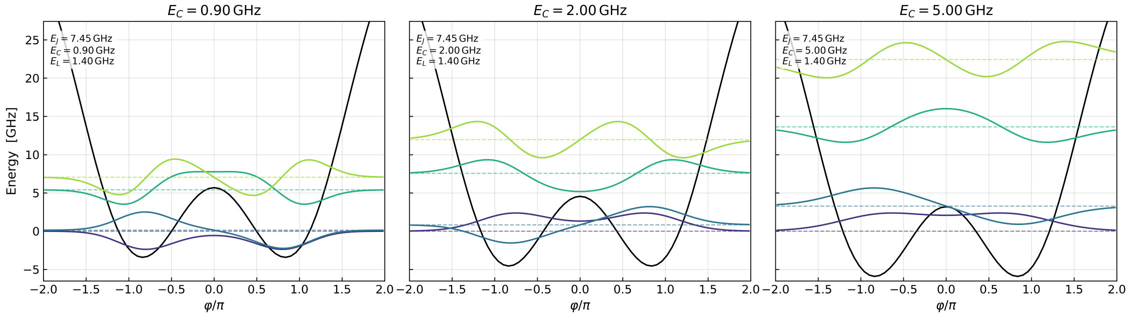

(b) Changing E_C while fixing other parameters at half flux quantum.

2.2.3 Matrix elements and selection rules

The coupling strength between eigenstates $|i\rangle$ and $|j\rangle$ under a drive is proportional to matrix elements of the phase $\hat{\phi}$ or charge $\hat{n}$ operators.

$$\Gamma_{ij}^{(\phi)} \propto \left|\langle i|\,\hat{\phi}\,|j\rangle\right|^2, \qquad \Gamma_{ij}^{(n)} \propto \left|\langle i|\,\hat{n}\,|j\rangle\right|^2. \tag{2.38}$$

Because the fluxonium potential $V(\hat{\phi}) = -E_J\cos(\hat{\phi} - \phi_{\mathrm{ext}}) + \frac{1}{2}E_L\hat{\phi}^2$ depends explicitly on the external flux ϕ_{ext}, *both* the eigenfunctions and the associated matrix elements vary periodically with ϕ_{ext}. At the sweet spot of half a flux quantum ($\Phi_{\mathrm{ext}} = \Phi_0/2$), even transitions such as $|0\rangle \leftrightarrow |2m\rangle$ become forbidden because of the symmetry of the wavefunctions (but if the qubit is coupled to a readout resonator, this restriction is lifted and the transitions can be driven [27]).

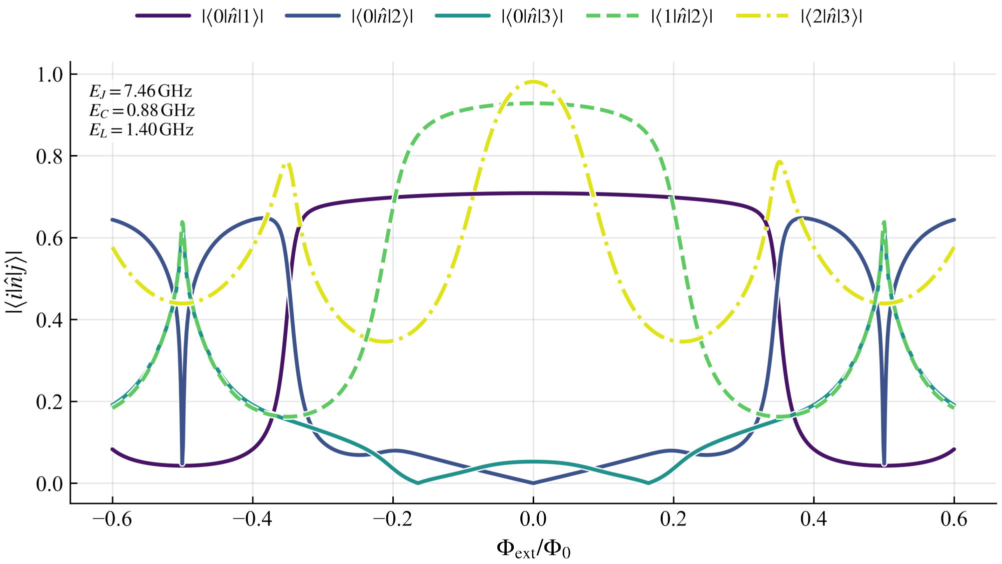

Figure 2.7: Plot of charge matrix elements across external flux. As discussed in the text, their values change drastically, some even becoming zero at certain points. Not surprisingly, the elements are symmetric around zero.

As can be seen from fig. 2.7, charge matrix elements are modifiable with external flux. This means, for capacitive coupling of the fluxonium to the waveguide, we can modify the rate at which an excitation decays to the environment. This feature makes the fluxonium appealing for applications in the field of Quantum Thermodynamics, as we can engineer the interactions with the environment in situ.

2.2.4 Superinductor

To satisfy the fluxonium parameter requirements, $E_L \ll E_J$ and $1 \lesssim \frac{E_J}{E_C} \lesssim 10$, an inductive energy $E_L = (\Phi_0/2\pi)^2/L$ of a few hundred megahertz, which translates into a *linear* inductance

$$L \gtrsim 100 \text{ nH}.$$

Such a large L must come with only a few femtofarads of stray capacitance; otherwise the self-resonant frequency $\omega_0 = 1/\sqrt{LC}$ would drop into the qubit band ($\omega_0/2\pi \lesssim 10$ GHz). The associated characteristic impedance $Z = \sqrt{L/C} \simeq 10^4\Omega$ therefore exceeds the resistance quantum (2.19) $R_Q = h/4e^2 \simeq 6.45$ kΩ. An inductor that satisfies $Z \gg R_Q$ over a broad microwave window and superconducts DC current is called a *superinductor* [28].
If we try to implement this type of inductance with geometric inductor, one will soon run into trouble. As electromagnetic fields are contained in the vacuum, the impedance of a geometric inductor is limited by vacuum impedance $Z_0 = \sqrt{\frac{\mu_0}{\epsilon_0}} = 377\ \Omega$. Instead, superinductance is achieved by using kinetic inductance: inductance associated to the momentum of charge carriers. Thus, this finiteness of momentum makes the acceleration time also finite, the same way in geometric inductors induced current opposes the change in magnetic flux. The two mechanisms are described

in the same way with inductors with inductance L. In superconductors, kinetic inductances can be achieved by nanowires [29], or by using long chains of Josephson junction(JJ) arrays[24].

2.2.5 Josephson junction array

In this thesis we adopt the JJ-array superinductor. As we know, in the lumped element approximation we can model a JJ as an inductor with inductance L_j (2.27) and capacitance C_j. JJ array would just be these components in series, each having a certain capacitance to ground C_g. (See Fig 2.8)

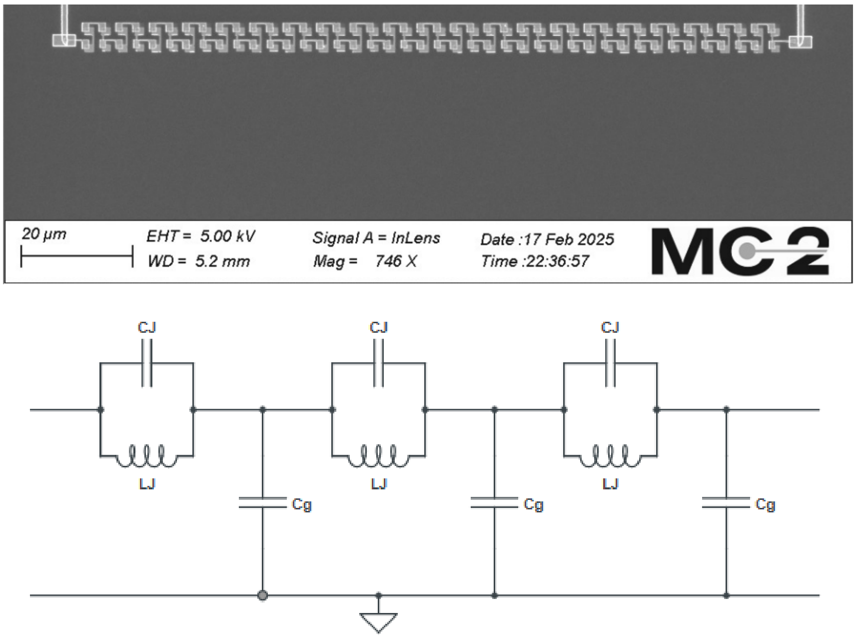

Figure 2.8: Josephson junction array used in the experiments (top) and the related circuit model (bottom). Each Josephson junction is treated as an inductor with inductance L_j and capacitance C_j. Stray ground capacitance to neighboring metallic objects also taken into account.

It is straightforward to see that for low frequencies this array would behave like inductors in series, giving a total inductance $L = NL_j$. But there is a limit to the number of junctions we can have. We can make a simple argument that as both total inductance and stray capacitance to ground scale with dimension of the array, the parasitic self-resonant mode $\frac{1}{\sqrt{LC_s}}$ gets smaller and would eventually lie in the band of interest. A more sophisticated analysis would include the Josephson Junction capacitances with a model given in Fig. 2.8 as well and we would finally arrive at this inequality for the number of JJs in an array [28]:

$$N \lesssim \frac{C_J}{C_g} \tag{2.39}$$

2.2.6 Fluxonium–waveguide coupling

We model the fluxonium (which we approximate here as a two-level system) coupled capacitively to a semi-infinite 50 Ω transmission line. The line contains input and output fields which satisfy the input-output relation given by

$$\hat{b}_{\text{out}}(t) = \hat{b}_{\text{in}}(t) + \sqrt{\Gamma_r}\,\hat{\sigma}_-(t). \tag{2.40}$$

Here Γ_r is the radiative decay rate of the qubit into the transmission line, and $\hat{\sigma}_-$ is the lowering operator of the excitation in the qubit.[30]
We define :

$$\Gamma_r : \text{ radiative decay into the 1D waveguide,}$$

$$\Gamma_{nr} : \text{ non-radiative (internal) decay,}$$

$$\Gamma_\phi : \text{ pure-dephasing rate.}$$

The total energy-relaxation and decoherence rates are

$$\Gamma_1 = \Gamma_r + \Gamma_{nr}, \qquad \Gamma_2 = \frac{\Gamma_1}{2} + \Gamma_\phi. \tag{2.41}$$

Then we would like to derive the reflection coefficient of our input coherent tone, and we closely follow [31]. A coherent probe with frequency ω_p driving the qubit gives rotating-wave approximation (RWA) Hamiltonian in the probe frame as:

$$\hat{H} = -\frac{\Delta}{2}\,\hat{\sigma}_z + \frac{\Omega}{2}\,\hat{\sigma}_x, \qquad \Delta \equiv \omega_p - \omega_{01}, \tag{2.42}$$

and Rabi rate Ω is given by the incoming field amplitude ($\Omega = 2\sqrt{\Gamma_r}\,|\alpha_{in}|$).
Including dissipation and dephasing, the density operator obeys

$$\dot{\rho} = -\frac{i}{\hbar}[\hat{H}, \rho] + \Gamma_1\,\mathcal{D}[\hat{\sigma}_-]\,\rho + \frac{\Gamma_\phi}{2}\,\mathcal{D}[\hat{\sigma}_z]\,\rho, \tag{2.43}$$

with the dissipator

$$\mathcal{D}[X]\rho = X\rho X^\dagger - \tfrac{1}{2}\Big(X^\dagger X\,\rho + \rho\,X^\dagger X\Big)\,.$$

Let

$$s_1(t) \equiv \langle\sigma(t)\rangle\,e^{i(\omega_p t - \theta_b)} \quad \text{and} \quad s_2(t) \equiv \langle\sigma^\dagger(t)\sigma(t)\rangle$$

From (2.43) one finds

$$\frac{d}{dt}\begin{pmatrix} s_1 \\ s_1^* \\ s_2 \end{pmatrix} = \begin{pmatrix} -\Gamma_2 + i\delta\omega & 0 & i\alpha\Omega \\ 0 & -\Gamma_2 - i\delta\omega & -i\alpha\Omega \\ i\alpha\Omega/2 & -i\alpha\Omega/2 & -\Gamma_1 \end{pmatrix}\begin{pmatrix} s_1 \\ s_1^* \\ s_2 \end{pmatrix} + \begin{pmatrix} -i\alpha\Omega/2 \\ i\alpha\Omega/2 \\ 0 \end{pmatrix}, \tag{2.44}$$

In steady state when ($\dot{s}_i = 0$) this yields

$$s_1 = \frac{\Omega\,\Gamma_1\,(\Delta - i\Gamma_2)}{2\,(\Omega^2\Gamma_2 + \Gamma_1(\Delta^2 + \Gamma_2^2))}\,. \tag{2.45}$$

The boundary condition is

$$\hat{b}_{\text{out}} = \hat{b}_{\text{in}} + \sqrt{\Gamma_r}\,\hat{\sigma}_-,$$

so for coherent drive $\alpha_{\text{in}} = \langle \hat{b}_{\text{in}} \rangle$, $\alpha_{\text{out}} = \langle \hat{b}_{\text{out}} \rangle$, and $\Omega = 2\sqrt{\Gamma_r}\,|\alpha_{\text{in}}|$, the complex reflection coefficient is

$$r(\omega_p) = \frac{\alpha_{\text{out}}}{\alpha_{\text{in}}} = 1 - \frac{i\,\Gamma_r\Gamma_1\,(\Delta - i\Gamma_2)}{\Omega^2\Gamma_2 + \Gamma_1(\Delta^2 + \Gamma_2^2)}\,. \tag{2.46}$$

With the equation (2.46) we can fit the experimental data and find out the coupling rates Γ_i. We can compare if their values follow the theoretically predicted trend given from eq(2.38). We will see more of that in the Results section.

3

Methods

This chapter describes the design–simulation–measurement pipeline used throughout the thesis. We begin with circuit design of the fluxonium (choosing E_J, E_C, E_L and the junction geometry) and its microwave environment (CPW resonator or semi-infinite 50 Ω waveguide). Full-wave EM simulations and energy-participation quantization give the Hamiltonian parameters. Then we follow by the cryogenic setup and spectroscopy protocols (CW and time-domain) and specifically the "magic-power" procedure to extract coupling rates and avoid saturation due to high power.

3.1 Design

The chip layout was drafted entirely in Qiskit Metal[32] and contains three fluxonium qubits arranged on a 7 mm × 7 mm, 8-port chip (Fig. 3.1):

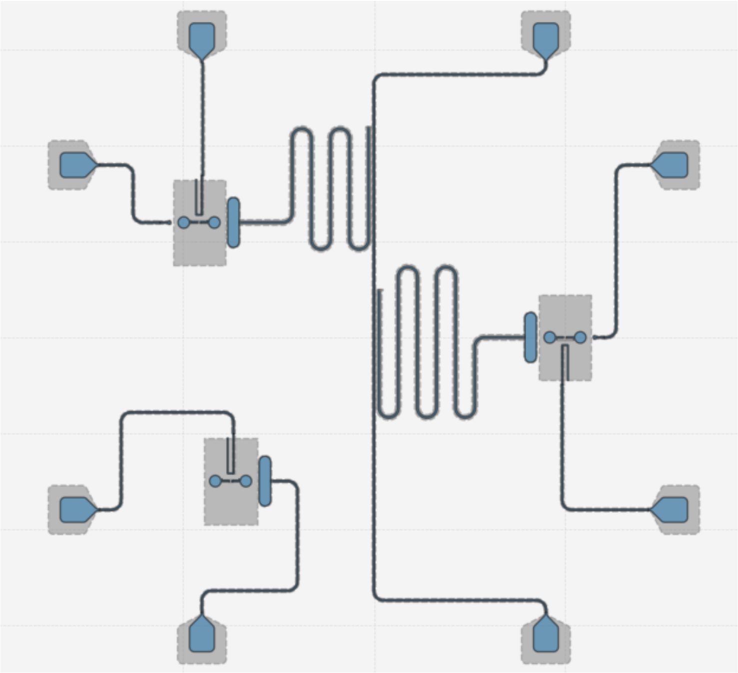

Figure 3.1: Qiskit Metal Design of the chip under the test

Qubit A and **Qubit B** couple capacitively to a shared $\lambda/2$ readout resonator positioned at the centre of the chip. Each of these qubits has its own single-ended *charge-drive* line for pulsed control and a dedicated *flux-bias* line for DC tuning.

Qubit C couples Capacitively to the semi-infinite feed-line that terminates at the right-hand edge of the chip. A separate flux line provides DC flux bias, but no microwave drive is applied through this line; The qubit will be driven via the waveguide.
All three devices share a common ground plane to minimise slot-line modes.

3.1.1 Junction Design

Accurate design of the Josephson junctions is critical for placing the fluxonium spectrum in its target window. Two separate junction topologies were employed:

3.1.1.1 Single junction (Manhattan layout)

The small junction used as a non-linear element of each fluxonium is patterned in a Manhattan cross geometry. The overlap area of the junction is 130 nm × 130 nm. This would correspond to the value of $E_j \simeq 5.6$GHz, which was the design value. The area to Josephson junction energy conversion comes from fitting done in each fabrication round.

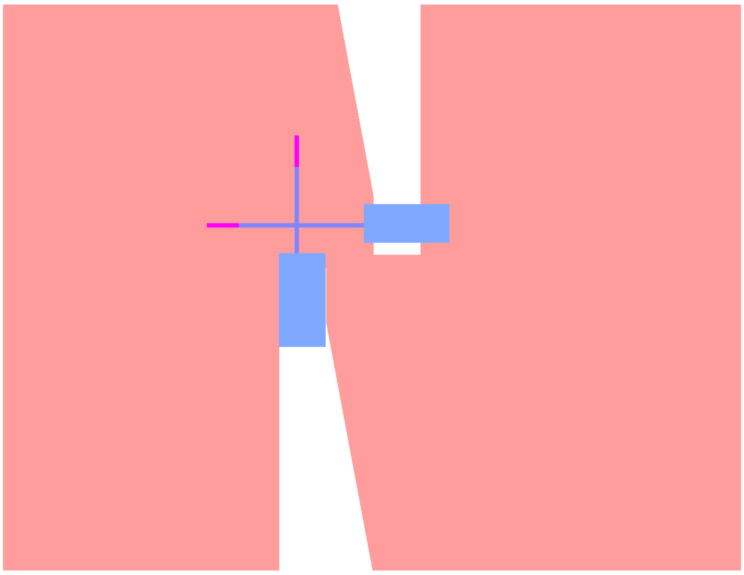

Figure 3.2: Design of 130 nm×130 nm Manhattan-style junction. Blue: junction; pink: undercut.

3.1.1.2 Superinductor array (Princeton style)

To realize the required $\sim 150\,\mathrm{nH}$ superinductance, we adopt the Princeton ladder junction layout introduced in [33]. The Al/AlO$_\mathrm{x}$/Al junctions are processed with a 1450 nm undercut and 960 nm shadow length (see fig 3.5), leaving an effective overlap of

$$A_{\text{array}} = 1450\,\mathrm{nm} - 960\,\mathrm{nm} = 490\,\mathrm{nm}.$$

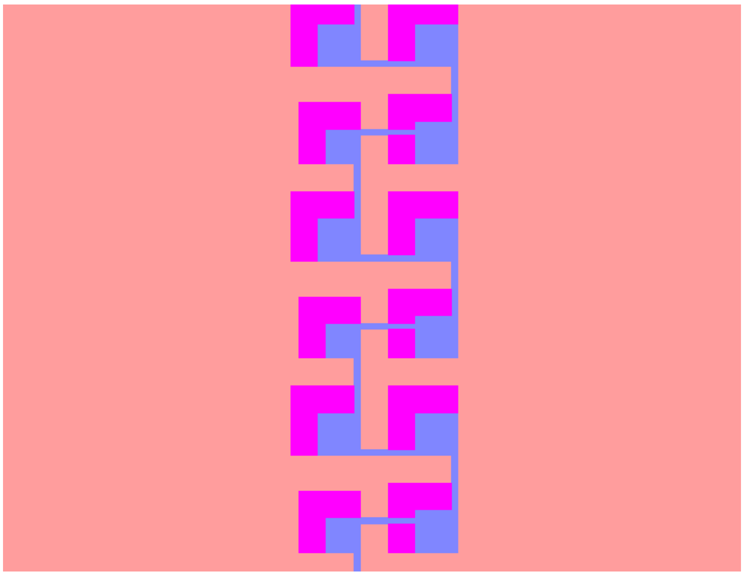

Figure 3.3: Design of 490x490 Princeton style junctions. Blue: Manhattan junction; Pink: undercut of the junction. The array consists of 100 junctions

This array size corresponds to

$$E_J^{\text{array}} \simeq h \times 104\,\text{GHz}.$$

With $N = 100$ identical junctions in series the linearized inductive energy is

$$E_L = \frac{(2e)^2}{\hbar}\frac{1}{L_{\text{array}}} = \frac{E_J^{\text{array}}}{N} \simeq h \times 1.04\,\text{GHz (or } L_{\text{array}} \approx 150\,\mu\text{H}),$$

matching the design target.

Table 3.1: Summary of junction parameters.

	Single junction	Array junction
Geometry	Manhattan cross	Princeton ladder
Nominal area (nm^2)	130×130	490×490
E_J/h (GHz)	5.6	104

The combination of a high-E_J single junction and a low-E_L, linearised array meets the dual requirement $E_L \ll E_J$ and $1 \lesssim E_J/E_C \lesssim 10$ for a strongly anharmonic but charge-noise-insensitive fluxonium qubit.

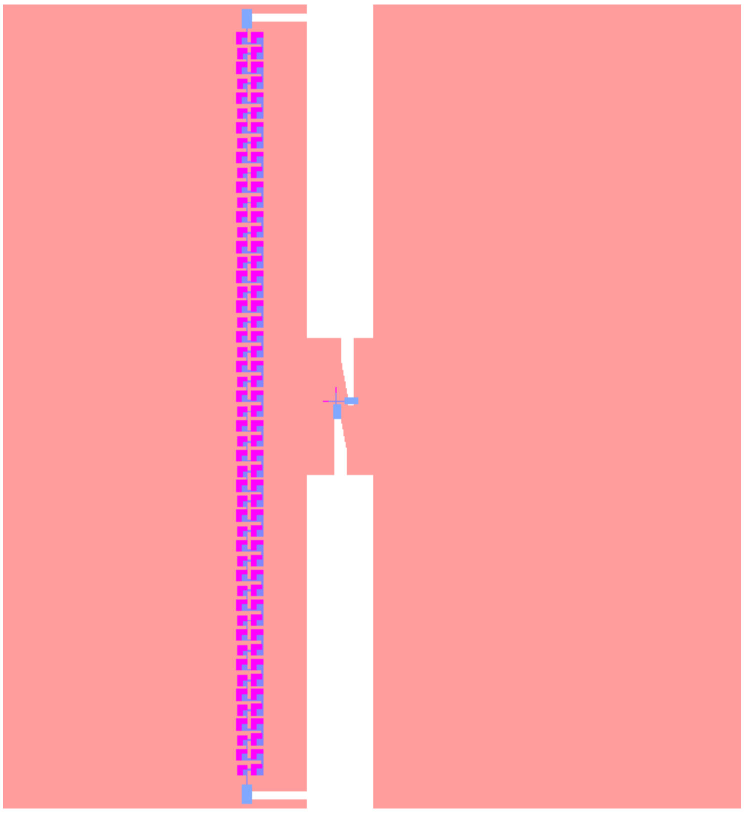

Figure 3.4: Josephson Junction array and single Josephson Junction side by side, connected to metallic pads which act as shunt capacitors

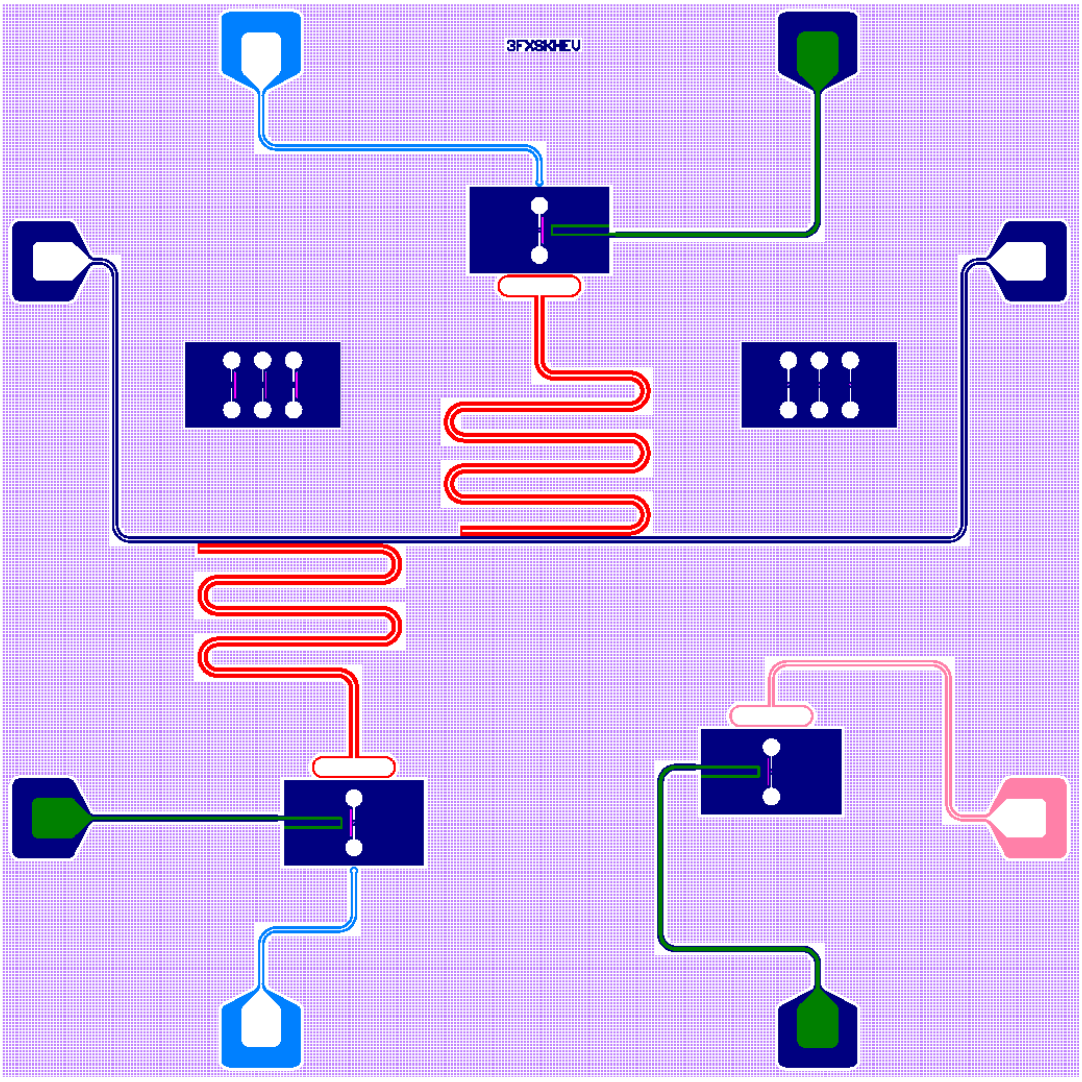

Figure 3.5: Final rendered design ready for simulation. Orange, light blue, green and pink components correspond respectively to readout resonators, qubit charge lines, qubit flux lines and a waveguide.

3.2 Simulation

All full-wave calculations were carried out in Ansys HFSS, called directly from the Qiskit Metal API.

3.2.1 Capacitance matrix and charging energy

All metal traces, ground pads, and Josephson-junction electrodes are exported as perfect electric conductors; air and substrate volumes inherit material properties from the Qiskit Metal design workspace. Each metal pad is assumed as a floating pad, while the common ground is set to 0V. HFSS solves $\nabla \cdot (\varepsilon \nabla V) = 0$ for every port excitation and returns the symmetric matrix $\mathbf{C}_{ij} = \partial Q_i / \partial V_j$.
The total island capacitance C_Σ is obtained by combining the HFSS pad–to–pad

Table 3.2: Reduced capacitance matrix (units: fF)

	charge pad	**top pad**	**bottom pad**	**ground plane**	**readout pad**
charge pad	23.128	-0.497	-0.065	-22.317	-0.033
top pad	-0.497	36.545	-3.584	-25.457	-1.061
bottom pad	-0.065	-3.584	36.529	-21.506	-5.732
ground plane	-22.317	-25.457	-21.506	327.801	-152.322
readout pad	-0.033	-1.061	-5.732	-152.322	163.192

values with the intrinsic junction capacitance C_J of the Al/AlO$_\mathrm{x}$/Al tunnel barrier ($\approx$ 50 fF/m^2 for a 130 nm junction, giving $C_J \simeq 0.85\,\mathrm{fF}$).

$$\begin{aligned} C_{\mathrm{top}} &= C_{\mathrm{pad,top}} + C_{\mathrm{charge,top}} + C_{\mathrm{fluxpad,top}} + C_{\mathrm{readout,top}} \\ &= 25.48 + 0.496 + 4.96 + 1.062 = 31.998\,\mathrm{fF}, \\ C_{\mathrm{bot}} &= C_{\mathrm{pad,bot}} + C_{\mathrm{readout,bot}} + C_{\mathrm{fluxpad,bot}} \\ &= 21.53 + 5.73 + 4.95 = 32.210\,\mathrm{fF}. \end{aligned}$$

The mutual pad capacitance $C_{\mathrm{pads}} = 3.613\,\mathrm{fF}$ adds in parallel, while the top/bottom networks combine in series:

$$C_\Sigma = C_J + C_{\mathrm{pads}} + \frac{C_{\mathrm{top}}\, C_{\mathrm{bot}}}{C_{\mathrm{top}} + C_{\mathrm{bot}}} = 33.87\,\mathrm{fF}.$$

The charging energy follows directly,

$$E_C = \frac{e^2}{2C_\Sigma} \quad\Longrightarrow\quad \frac{E_C}{h} = \frac{e^2}{2hC_\Sigma} \simeq 0.943\,\mathrm{GHz}.$$

3.2.2 Eigenmode solver and Energy Participation Ratio

In the second pass the fluxonium pads are shorted by linear inductors of value $L_J = (\Phi_0/2\pi)^2/E_J$; With HFSS then we will proceed to solve the classical Maxwell eigenproblem

$$\nabla \times \left(\mu^{-1}\nabla \times \mathbf{E}\right) = \omega^2\varepsilon\mathbf{E},$$

subject to perfect-conductor and radiation boundaries. Each eigenvalue ω_k then will yield a mode's complex field profile $\mathbf{E}_k(\mathbf{r})$.

After running the simulations for 3 different systems, we see that the converged modes are as shown in Table 3.3.

However, these frequencies are only an approximation, since instead of the non-linear inductor we are using a normal linearised inductor. To overcome this issue, we use what is called the energy-participation-ratio (EPR) routine [34]. Here, we first calculate with classical simulations what is called the participation ratios:

$$p_m \;:=\; \frac{\text{Inductive energy stored in the junction}}{\text{Total inductive energy stored in mode } m},$$

Table 3.3: Lowest five eigenmodes of the linearised model (linear inductors in place of Josephson junctions).

Mode	$\omega_k/2\pi$ (GHz)	Assignment
1	5.83	Fluxonium C (waveguide-coupled)
2	5.83	Fluxonium A (resonator-coupled)
3	5.84	Fluxonium B (resonator-coupled)
4	7.43	Read-out resonator A, $\lambda/2$
5	5.65	Read-out resonator B, $\lambda/2$

evaluated when only mode m is excited. In the quantum picture one can write

$$p_m = \frac{\left\langle \psi_m \middle| \frac{1}{2} E_J \hat{\varphi}_J^2 \middle| \psi_m \right\rangle}{\left\langle \psi_m \middle| \frac{1}{2} \hat{H}_{\text{lin}} \middle| \psi_m \right\rangle}, \tag{3.1}$$

where $|\psi_m\rangle$ denotes a single-photon Fock excitation of mode m.

If we simplify Eq. (3.1) (see Supplementary Sec. A6 of Ref. [34]) we obtain the zero-point phase fluctuations for modes of interest, in this case a resonator mode (r) and a qubit mode (q), or only the qubit mode:

$$\varphi_r^2 = p_r \frac{\hbar\omega_r}{2E_J}, \qquad \varphi_q^2 = p_q \frac{\hbar\omega_q}{2E_J}.$$

where ω_q and ω_r are the frequencies found in the previous step in eigenmode simulations. If we have the zero point fluctuations, we can construct a full Hamiltonian by noting the following relations:

$$\hat{H}_{\text{full}} = \hat{H}_{\text{lin}} + \hat{H}_{\text{nl}}, \tag{3.2}$$

$$\hat{H}_{\text{lin}} = \hbar\omega_c\, \hat{a}_c^\dagger \hat{a}_c \;+\; \hbar\omega_q\, \hat{a}_q^\dagger \hat{a}_q, \tag{3.3}$$

$$\hat{H}_{\text{nl}} = -E_J \left[\cos(\hat{\varphi}_J - \varphi_{ext}) + \frac{\hat{\varphi}_J^2}{2} \right], \tag{3.4}$$

$$\hat{\varphi}_J = \varphi_q\, (\hat{a}_q + \hat{a}_q^\dagger) + \varphi_r\, (\hat{a}_r + \hat{a}_r^\dagger), \tag{3.5}$$

After this, the common way to numerically diagonalize the Hamiltonian is to expand the cosine term up to the fourth order. This way works with weakly anharmonic qubits, like transmons. However, when the qubit is highly non-linear, like fluxonium, we need to include terms of higher order[35][36]. Then, the full Hamiltonian is diagonalized and modes involving qubit and resonator(if we have a resonator coupled) are identified.

Table 3.4: EPR-corrected mode frequencies at zero flux and at the half-flux sweet spot ($\Phi_{\text{ext}} = \Phi_0/2$).

Device / mode	$f_{\text{EPR}}(0)$ (GHz)	$f_{\text{EPR}}\big(\Phi_0/2\big)$ (GHz)
Fluxonium A	6.13	0.21
Fluxonium B	6.14	0.24
Readout resonator A	7.43	7.43
Readout resonator B	5.66	5.66
Fluxonium C	6.14	0.23

3.3 Cryogenic Measurements

3.3.1 Measurement setup

As discussed in the theory section, resolving quantum energy levels in superconducting circuits requires operation at millikelvin temperatures such that $k_{\text{B}}T \ll \hbar\omega_{01}$ (see Eq. 2.22). We therefore use dilution refrigerators, which reach these temperatures via mixing of ^{3}He and ^{4}He [37]. In such setups, wiring to the device runs from the mixing chamber (MXC at around 10mK) up to room-temperature electronics, unavoidably introducing both passive heat loads (arising from thermal conduction in metals and also noise from warmer stages) and active heat loads (heating and dissipation in attenuators, filters, and other components that carry signals). Without adequate attenuation and filtering, thermal radiation dephases the device and stray high-frequency photons can even generate nonequilibrium quasiparticles in superconductors [38].

In practice, cryostat wiring is organized in two different categories that require different approaches. DC lines carry current to the mixing chamber, usually in a twisted pair arrangement. In our case, we use the twisted pair setup to bias with the DC voltage at room temperature. The twisted pair setup converts to a coaxial cable at the mixing chamber, and then it is directly connected to the device. DC lines are used for primarily two reasons: biasing the components used in the wiring (for example amplifiers) or delivering current close to device, which generates flux and changes the frequency of the qubit, as is in our case. Therefore fluctuations in current would lead to dephasing of our qubit, which is why filtering DC lines is often a good idea.

RF (microwave) lines connect room-temperature electronics to the device and they also deliver clean control pulses. In order to meet these requirements, the lines are attenuated and filtered carefully and are thermalized at each cryostat plate. Drive lines deliver qubit and readout pulses from room temperature to the chip. A typical configuration uses coax cables with cryogenic attenuators distributed across stages. Readout lines extract the weak microwave field that encodes the device state. Con-

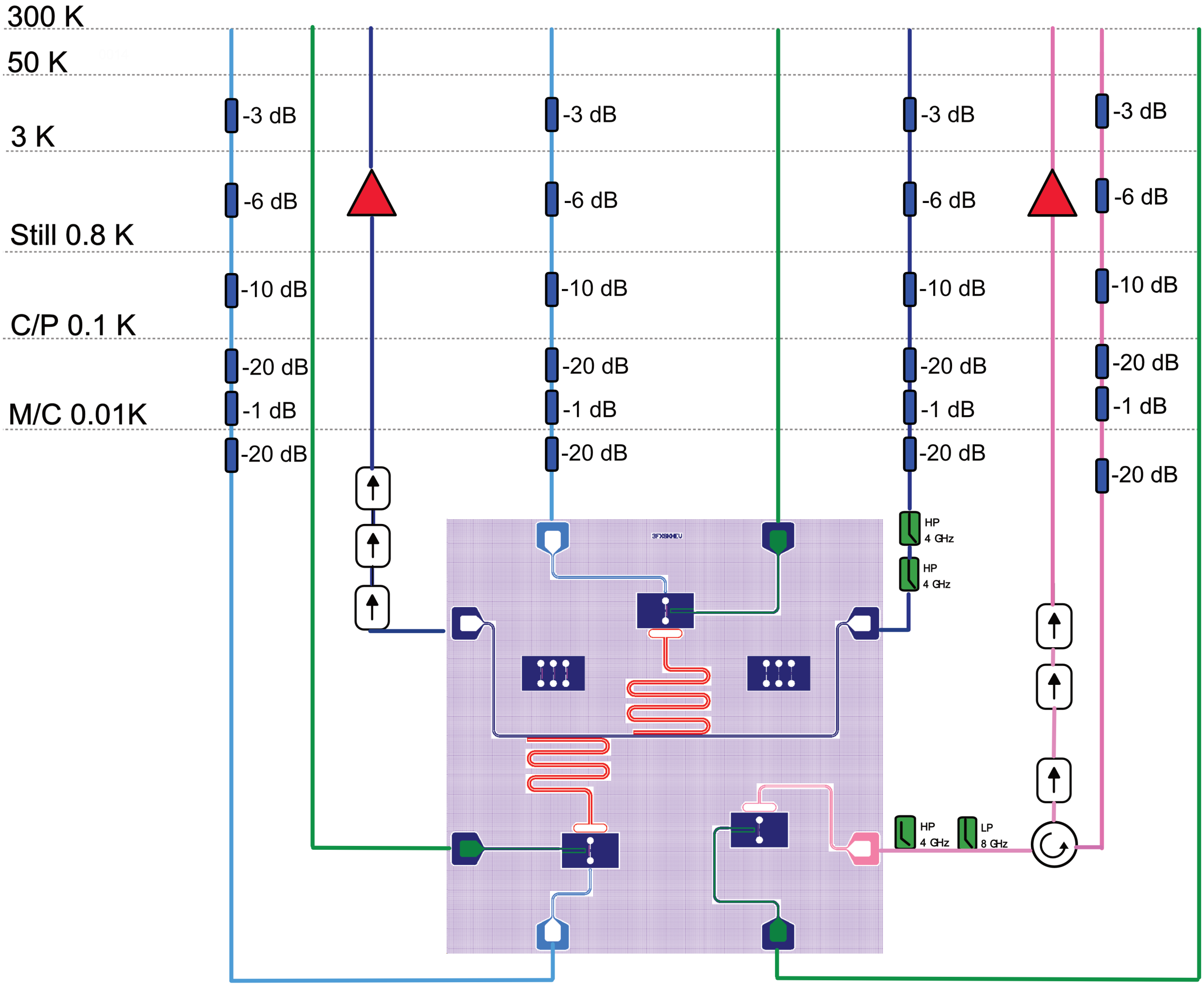

Figure 3.6: Wiring diagram of the dilution refrigerator used in the experiments. Green (DC) lines connect to on-chip flux lines; light blue to charge lines; pink to the waveguide; dark blue to the transmission line coupled to two resonators.

trary to the case of drive lines, they avoid attenuation near the device which is crucial to have a good signal to noise ratio. Two or three isolators/circulators are typically placed from MXC up to the 600–800 mK stage, followed by a cryogenic HEMT amplifier at 4 K and, if available, quantum-limited amplifier at base (JPA/JPC or a JTWPA).

3.3.2 Experimental techniques

In order to find out if the device is meeting our design targets, we need to characterize it. For characterization, we used two different techniques: continous wave (CW) spectroscopy, which probes the steady state response of the system in the frequency domain, and time-domain measurements, which resolve system dynamics with short and shaped microwave pulses.

3.3.2.1 Continous wave spectroscopy

In CW spectroscopy, we probe the linear, steady–state response of the chip with continuous tones while recording complex scattering parameters. In this work, we used *one–tone* spectroscopy to characterize the readout resonators and the waveguide qubit in reflection and *two–tone* spectroscopy to locate qubit transitions. We also did the VNA *power dependence* measurement to determine an optimal ("magic") power, which corresponds to the optimal dip while avoiding broadening due to high power.

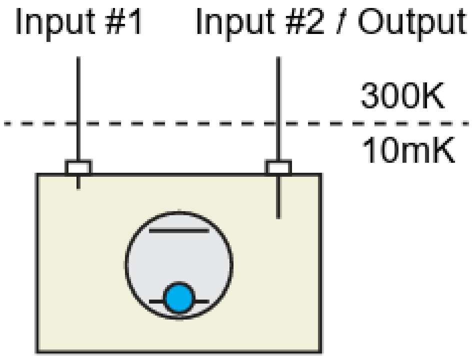

Figure 3.7: Schematic of a continuous wave spectroscopy with a VNA. This setup can work for a measurement in reflection, as well in transmission. Taken from [1]

We have two $\lambda/2$ resonators, the complex response near the resonance is well described by

$$S_{21}(\omega) = a\, e^{i\theta}\left[1 - \frac{Q_\ell}{Q_c}\,\frac{e^{i\phi}}{1 + 2iQ_\ell x}\right], \qquad x \equiv \frac{\omega - \omega_r}{\omega_r}, \tag{3.6}$$

where $Q_\ell^{-1} = Q_i^{-1} + Q_c^{-1}$ and ϕ describes the physics for impedance asymmetries in the feedline [39]. Fitting Eq. (3.6) (circle method) yields ω_r, Q_i, and Q_c. For the waveguide–coupled qubit geometry, we already have a model given in the theory section using Eq. (2.46).

After finding out the resonator frequency we can move to the Two-Tone measurements. With the readout probe fixed on the resonator peak, we sweep the qubit drive frequency. At the frequency of qubit, the resonator will get displaced, causing the probe to get displaced from the dip, resulting in a peak. This is a crude way to extract qubit frequency for characterization.

For the Magic Power measurement, the goal is to choose a probe power that maximizes resonance response without causing power broadening. In steps we need to:

1. **Acquire a power sweep.** Record complex traces $S_{11}(\omega; P_k)$ over the same frequency span in a sweep of powers P_k (from well below to above the expected operating range). This may require increased averaging at lower powers.

2. **Baseline removal.** For each P_k, we remove the baseline measurement from it.

3. **Depth metric and selection.** Pick the *magic power* $P^\star$ that maximizes the peak depth.

4. **Final fit at $P^\star$.** Fit the reflection data at magic power $S_{11}(\omega; P^\star)$ to the formula given in Eq. (2.46)

3.3.2.2 Time domain measurements

In time domain measurements, we use the same scheme for control and for readout. An arbitrary waveform generator (AWG), which is limited in high-frequency generation, synthesizes quadrature envelopes at intermediate frequency, $I_{\mathrm{IF}}(t)$ and $Q_{\mathrm{IF}}(t)$, which go into the ports of an IQ mixer together with a local oscillator pulse with frequency ω_{LO}. This process, known as upconversion, produces a narrowband pulse at $\omega_{\mathrm{RF}} = \omega_{\mathrm{LO}} \pm \omega_{\mathrm{IF}}$ (depending on if we use upper or lower sideband). The resultant RF pulse propagates down the attenuated line into the cryostat, couples to the resonator or waveguide and is transmitted or reflected back.

The same process can also work in reverse: on the way back, the same LO is used to pump a second IQ mixer. In this mixer, the RF port is the input and we recover the intermediate frequencies $I_{\mathrm{out}}(t)$ and $Q_{\mathrm{out}}(t)$ that the digitizer records. This step is crucial as the digitizer can't sample frequencies far in the GHz range. Using the same LO has the benefit of keeping the phase fixed. Typical values of IF frequencies are between $50-300$ MHz.

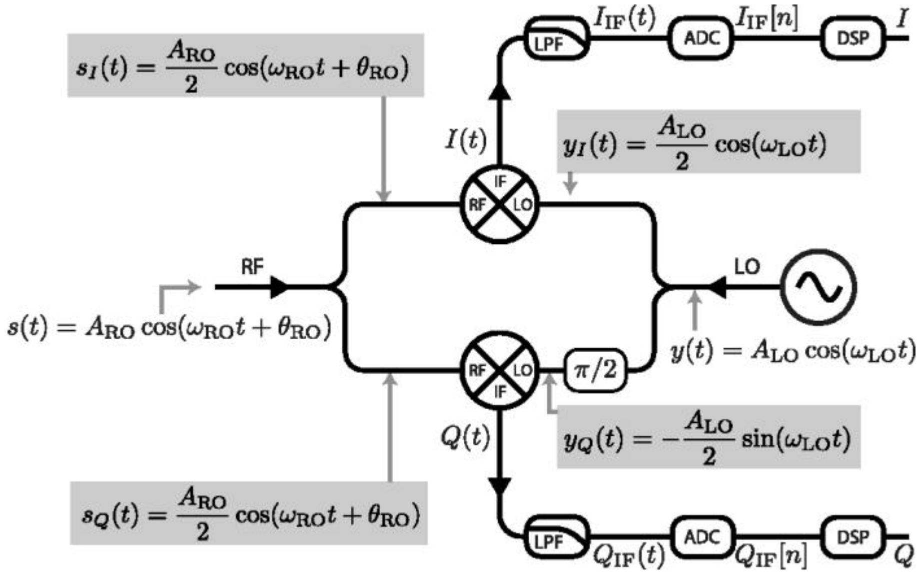

Figure 3.8: IQ downconversion chain: the RF readout tone is mixed with in-phase and 90°-shifted LO signals to yield I/Q IF outputs, then low-pass filtered, digitized, and DSP-processed. Figure taken from [2]

4

Results

This chapter presents the experimental results. We first characterize the device coupled to the resonator, using single- and two-tone spectroscopy. Results confirm the expected flux dependence and dispersive coupling. We then move on to the waveguide-coupled device (on which most experiments were conducted), where flux dependence of the 0-1, 0-2, 1-2, and 0-3 transitions are acquired. We fit the reflection with an input-output model to separate radiative and non-radiative decay rates. Finally, the flux regime where Γ_{01} is strongly suppressed while Γ_{02} and Γ_{12} remain large is identified. This flux regime is suitable to realize a Λ-type system.

4.1 Characterizing resonator-coupled atoms

After finding the resonator mode, we perform *punchout* measurement to verify the Josephson junction of qubit has been realized. The idea is simple: sweep the readout power while measuring the scattering parameter $S_{21}(\omega)$ over a narrow frequency range about the resonant frequency of a resonator. After the power injected in the Josephson junction increases beyond a threshold, the critical current. At this point, we observe the bare frequency of the cavity. The figures 4.1 confirm the Josephson junction is operational and we have a non-linearity in the system.

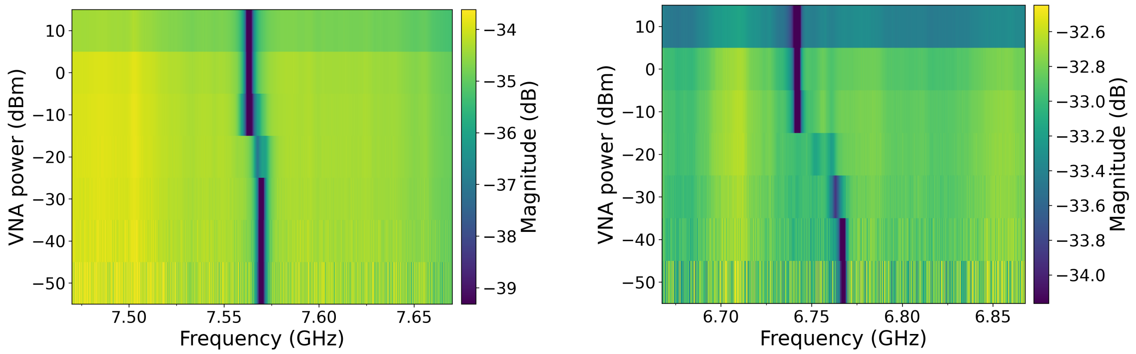

Figure 4.1: Punchout measurements for the two readout resonators coupled to qubits A (left) and B (right) | We see a clear shift in frequency with high power.

Next step, to see that the fabrication of Josephson junction array was successful and there were no cuts in it, we try to see the flux dependence of the resonator frequency. We know theoretically that the frequency of the fluxonium atom changes with external flux that threads the loop. As fluxonium and the cavity are coupled, the change in fluxonium frequency also shifts the cavity frequency. Thus, if we see a cavity frequency change with external flux, this would confirm the JJ array is functional.

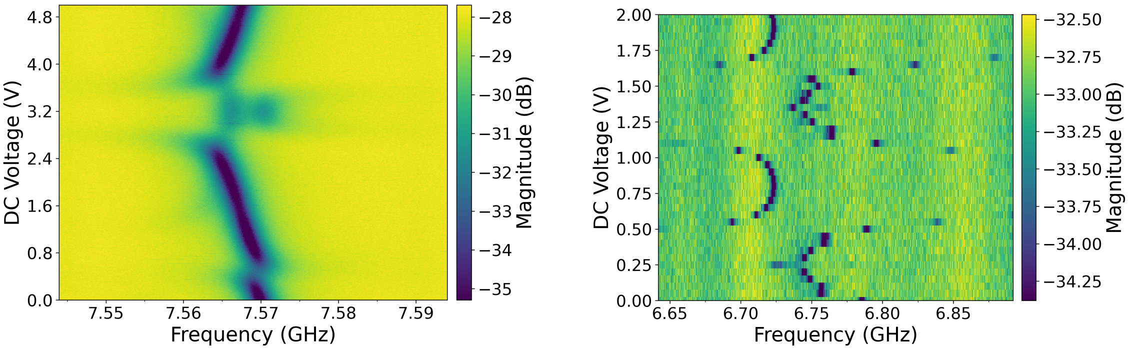

Figure 4.2: Flux dependence of fundamental mode of resonators A (left) and B (right) | Variation of resonator frequency confirms Josephson junction array has no cuts and the loop is formed through which the flux is threaded. We can clearly see different periodicity, which is arising due to different resistances on the flux line.

Other interesting feature of the Fig. 4.2 is the avoided crossings. They appear because at that specific flux point one of the fluxonium transition frequencies has the value close to the resonator frequency, and thus modes hybridize.

Before we move to the time-domain measurements, it is important we identify the qubit frequency. For this, we do a two tone measurement discussed in Subsec. 3.3.2.1. This gives a crude but fast way to extract qubit frequency, which will save a lot of time later in time-domain measurements. The results of these measurements are summarized in Fig. 4.3. We see that the fluxonium frequency shifts with external flux, as expected.

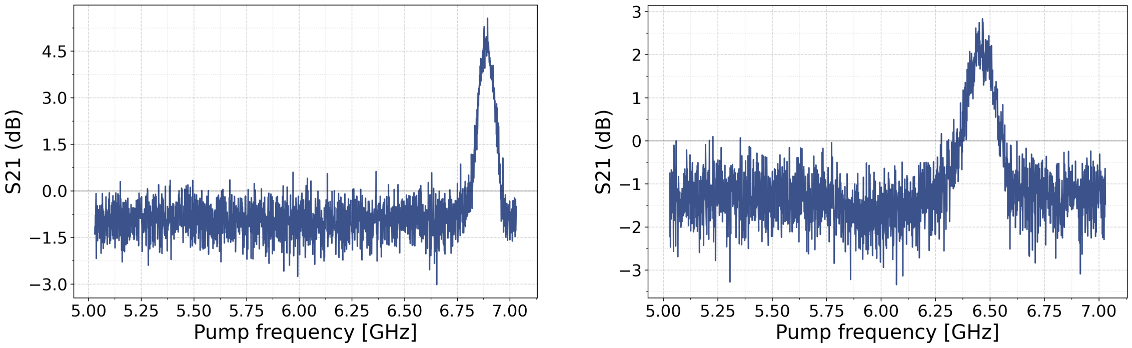

Figure 4.3: Two-tone measurements of qubit-resonator system A | Qubit mode detected as a peak in scattering parameter S_{21} for flux biasing voltage at 0 V (left panel) and 2 V (right panel).

After identifying JJ and JJ array are functional, we move to time domain measurements. In order to find the qubit frequency, first we need to identify the resonator coupled to the transmission line.

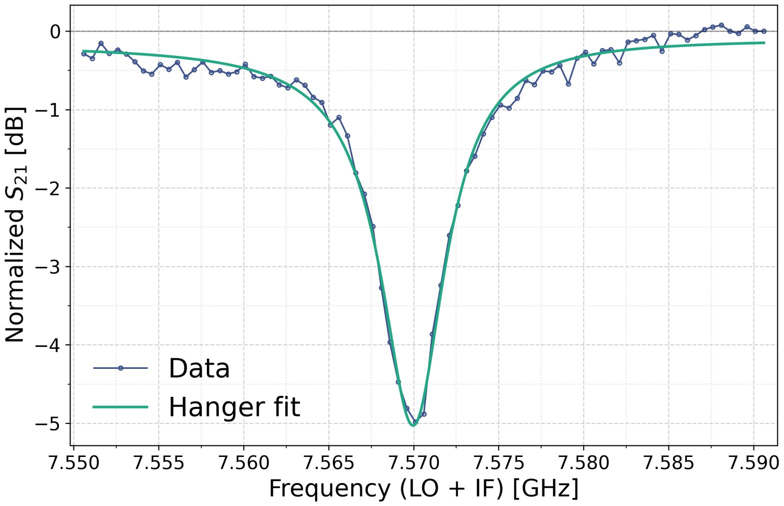

Figure 4.4: Measured transmission S_{21} (dark markers) resonator A together with a theoretical hanger fit (lighter line) | The extracted resonance frequency is $f_0 = 7.57$ GHz, with coupling rate $\kappa_c/2\pi = 2.66$MHz and internal loss rate $\kappa_i/2\pi = 3.50$MHz, yielding a total decay rate $\kappa_{\text{tot}}/2\pi = 6.16$MHz.

After identifying the resonator frequency, we move on to the two-tone measurements. The principle is the same as in continuous-wave measurements: we record the time trace of the resonator while varying the pump frequency to the qubit. After identifying the transition frequency of the qubit, we can do a dispersive shift measurement while varying the long pulse amplitude to the qubit. The resonator fundamental frequency will shift dispersively depending on the amplitude, reaching the biggest shift when qubit is fully excited.

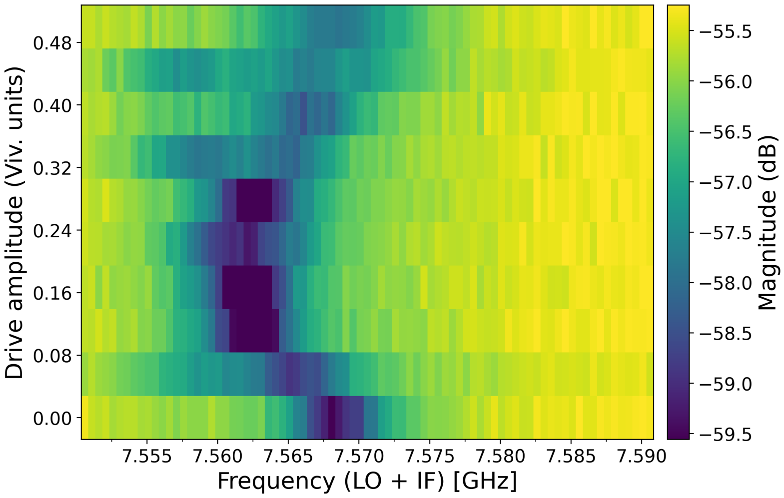

Figure 4.5: Two-dimensional map of resonator A response as a function of qubit drive amplitude | The shift in the fundamental frequency is observed as qubit gets excited.

4.2 Characterizing waveguide-coupled atom

4.2.1 0-1 and 0-2 transitions

After characterizing the resonator coupled qubit system, we move to characterization of qubit coupled to the waveguide. In order to find the transitions, one has to be extremely careful checking the spectrum at different external flux points. This is because trapped flux, which is common in superconducting chips, can shift the fluxonium spectrum. Therefore, at zero applied voltage we may not really be at fluxonium's sweet spot $\Phi_{ext} = 0$ and transitions may be harder to locate. For atoms coupled to the waveguide we can find the frequencies with a continuous one-tone measurement. The power also has to be chosen carefully, so that the transition is visible, but we are not sending too much power that would cause saturation.

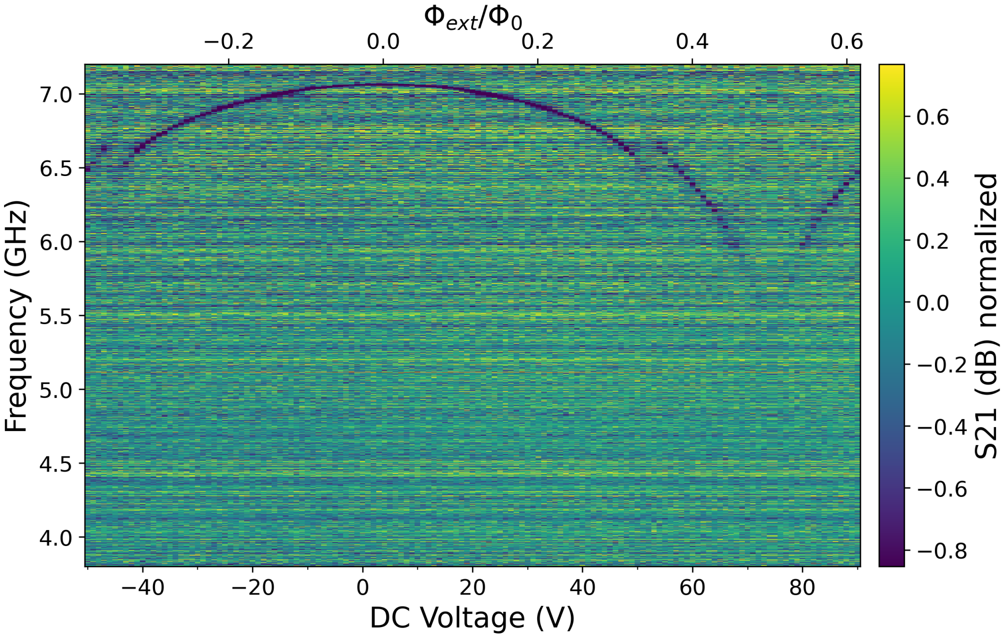

Figure 4.6: One tone measurement of a fluxonium coupled to a waveguide | We can clearly see fluxonium 0-1 and 1-2 transitions: as 0-1 transition fades 0-2 appears.

As can be seen from Fig. 4.6, transitions disappear for certain flux points. This can be explained both by decreasing of coupling to the waveguide due to modified matrix elements (see Fig. 2.7) and increased dephasing due to flux noise. Near the flux operating point at which the 0-1 transition matrix element decrease, transition 0-2 appears, consistent with the experiment.

4.2.2 1-2 transition

To probe the transition 1-2, we perform two-tone measurements. We apply a constant pump at 0-1 frequency and then measure the S21 characteristic to search for the 1-2 transition. Because 0-1 transition changes for each flux point, we also need to change the pump frequency.

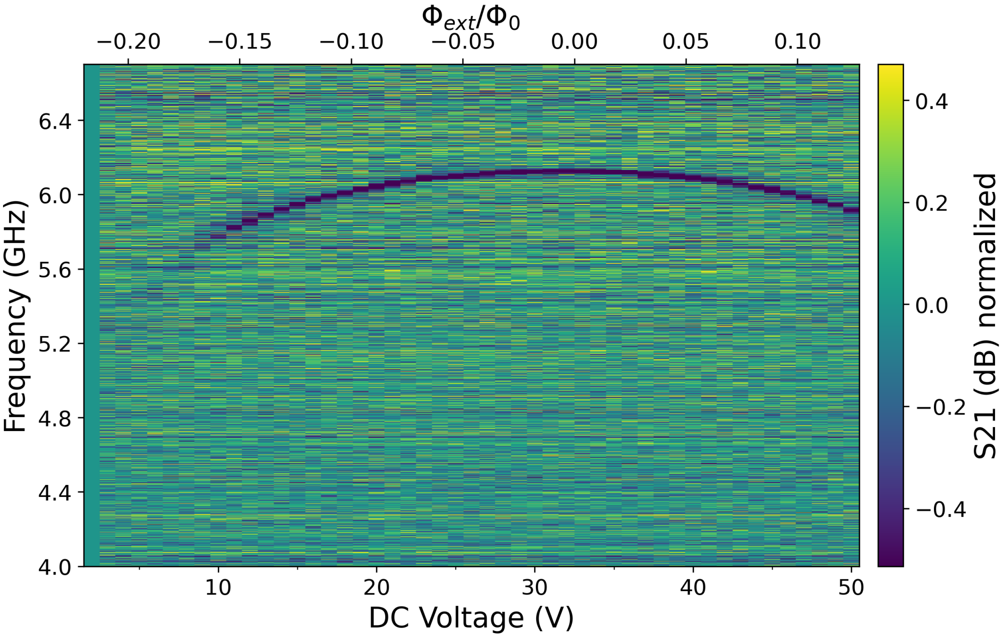

Figure 4.7: Normalized transmission S_{21} of the waveguide fluxonium device versus DC bias voltage and probe frequency | The background at 2 V has been subtracted. As like with 0-1 and 0-2 transitions we see that after certain flux points transition disappears.

As seen in Fig. 2.7, the simulated matrix element for the 1-2 transition decreases faster than for transition 0-1, which explains why it fades out while transition 0-1 is still visible.

4.2.3 0-3 transition

We can see from Fig. 2.7 that 0-3 has a really small matrix element everywhere besides the sweet point $\Phi_{ext} = \Phi_0/2$. Therefore, it is hard to locate it experimentally except near this point. Also, this transition was visible only during one cryostat cooldown, suggesting the wiring configuration strongly affects the visibility of energy levels.

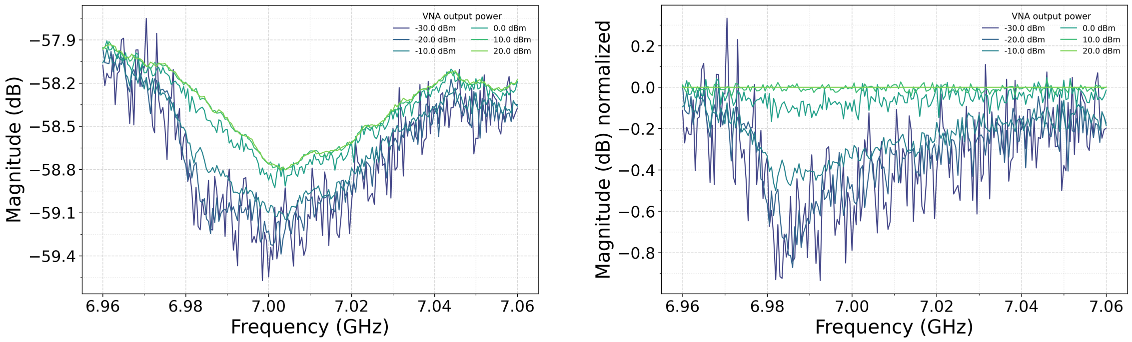

Figure 4.8: One tone measurements locating the 0-3 transition of a fluxonium coupled to a waveguide showing raw data (left) and normalized data to background (right) | As we increase the power, we saturate the transition with photons until the response is no longer visible.

4.2.4 Fitting the data

After finding all transitions, we combine them and fit the transition spectrum to the theoretically calculated eigenenergies of the Hamiltonian in Eq. (2.37). Each transition must be renormalized to the same flux axis, as setups can differ in flux-line resistance; the same voltage can correspond to different flux values (and different cryostat cooldowns can trap different amounts of flux).

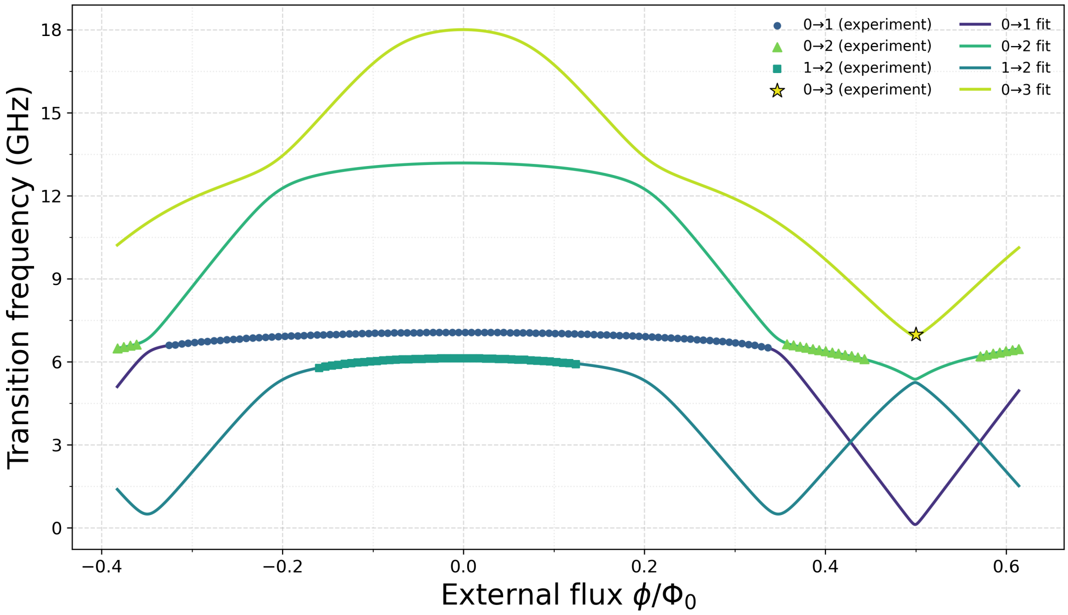

Figure 4.9: Measured fluxonium transition frequencies ($0\to1$, $0\to2$, $1\to2$, and $0\to3$) as a function of normalized external flux, together with a fit to the fluxonium Hamiltonian | Circles, triangles, squares, and the star correspond to experimental data points for the respective transitions, while solid lines show the best-fit theoretical curves. The extracted parameters are $E_C = 0.87\text{GHz}$, $E_J = 7.49\text{GHz}$ and $E_L = 1.41\text{GHz}$.

4.3 Extracting atom-waveguide coupling

As explained in the subchapter 3.3.2.1 we characterize the decay rates of fluxonium artificial atom to the waveguide using a power dependence measurement. The data from these measurements are fitted to Eq. (2.46) and coupling rate is extracted. We do this for 0-1 transitions as well as 0-2 transitions. Before proceeding, we note that fitting to Eq. (2.46) does not distinguish between Γ_{nr} and Γ_{ϕ}. Therefore, we set $\Gamma_{\phi} = 0$, and the sum of these contributions is represented as a single decay rate Γ_{nr} obtained from the fit.

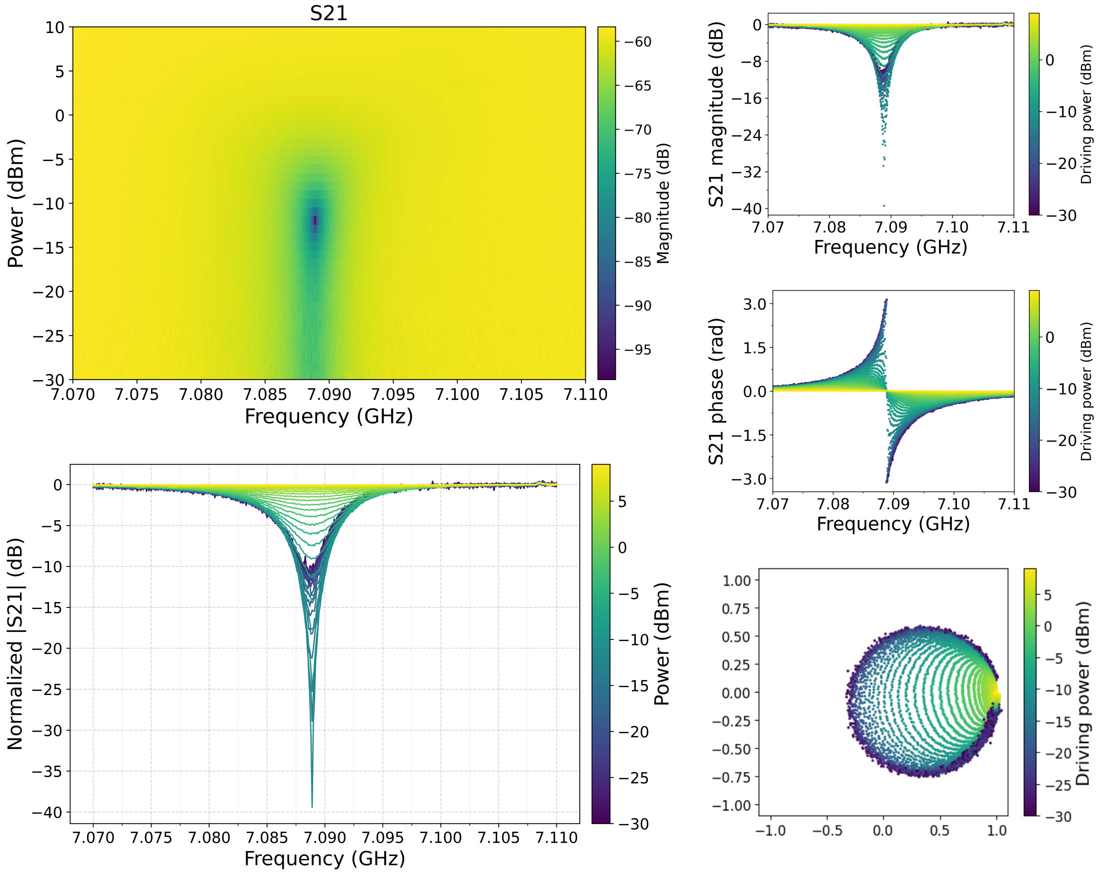

Figure 4.10: Magic power measurement and power sweep for a fluxonium atom 0-1 transition coupled to a waveguide | From the fit to the measured reflection coefficient, the extracted decay rates are $\Gamma_{\mathrm{r}}/2\pi = 4.49$ MHz (radiative), $\Gamma_{\mathrm{nr}}/2\pi = 2.48$ MHz (non-radiative), and total $\Gamma/2\pi = 6.98$ MHz.

As we can see from Fig. 4.10 and Fig. 4.11 we fit the extracted data to find the radiative rate into the line and the non-radiative decay, which accounts for internal loss and dephasing. The 0–1 line shows a narrow, well-behaved resonance with modest non-radiative decay. In contrast, the 0–2 line is noticeably broader and shallower; the extracted non-radiative contribution is roughly an order of magnitude larger than for 0–1.

Two effects are consistent with this observation. First, the 0–2 transition is more flux-dispersive at our operating bias: its frequency changes more steeply with external flux than 0–1, so flux fluctuations cause more energy level broadening. Second, relaxation from the second excited state has additional pathways. Population can decay not only directly to the ground state but also via the intermediate state (2-1-0). This opens extra internal loss channels for 0–2 that are not present for 0–1 and raises the apparent non-radiative rate.

To determine which pathway is more dominant in the 0–2 case—dephasing or internal loss—we examine the flux point corresponding to the 0–2 transition frequency shown in Fig. 4.11 (see Fig. 4.13). At this point, we would expect the 0–2 and 1–2 decay rates to be of similar magnitude. Consequently, the internal decay from level 2 to 1 should be of the same order as the 0–2 radiative decay rate obtained from the fit. However, Γ_{nr} is an order of magnitude larger than Γ_r, which strongly suggests that the dominant pathway is dephasing due to flux noise.

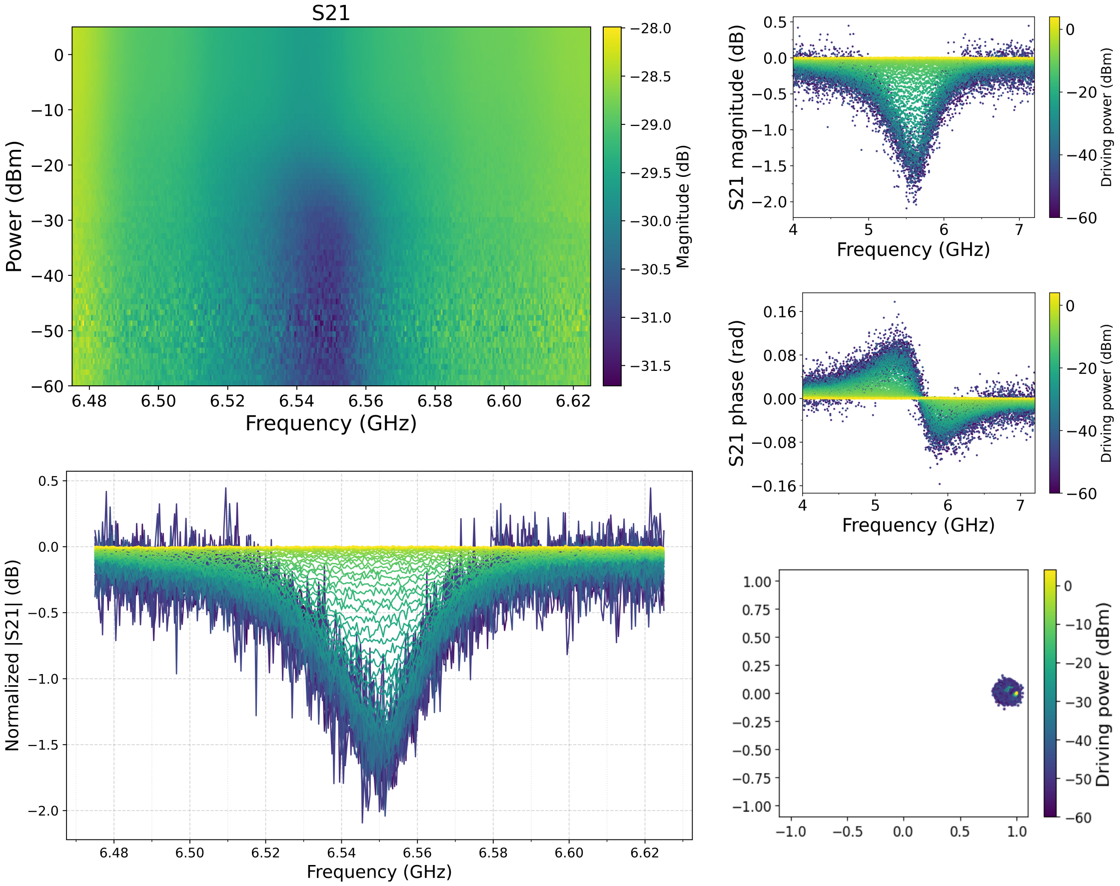

Figure 4.11: Magic power measurement and power sweep for a fluxonium atom 0-2 transition coupled to a waveguide | From the fit to the measured reflection coefficient, the extracted decay rates are $\Gamma_\mathrm{r}/2\pi = 2.30$ MHz (radiative), $\Gamma_\mathrm{nr}/2\pi = 31.35$ MHz (non-radiative), and total $\Gamma/2\pi = 33.65$ MHz.

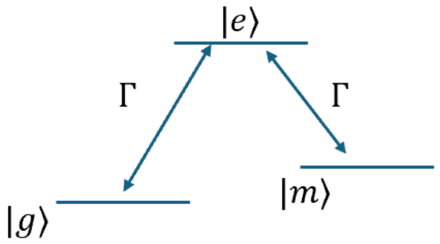

Figure 4.12: Schematic of a Λ three-level system, with two lower states $|g\rangle$ and $|m\rangle$ both coupled to a common excited state $|e\rangle$ via transitions of equal strength Γ, while direct coupling between $|g\rangle$ and $|m\rangle$ is negligible.

4.4 Λ system with fluxonium coupled to waveguide

A Λ system is a three-level quantum system with two "lower" states $|g\rangle$ and $|m\rangle$ and one common excited state $|e\rangle$. In a lambda system $|g\rangle \leftrightarrow |m\rangle$ coupling is negligible, while $|g\rangle \leftrightarrow |e\rangle$ and $|m\rangle \leftrightarrow |e\rangle$ is allowed, and usually coupling Γ is engineered to be the same.

4.4.1 Choosing flux point for Λ system

For fluxoniums, we know that at symmetry points, eigenstates possess definite parities that yield strong selection rules. Slightly away from these points, parity is weakly broken and the matrix elements of charge and flux operators become tunable.
We choose $|0\rangle$, $|1\rangle$ and $|2\rangle$ states of fluxonium coupled to waveguide to engineer a lambda system, where $|0\rangle$ and $|1\rangle$ are "lower" states and $|2\rangle$ is a common excited state. This can be engineered in our system that is coupled capacitively to the by moving to a flux point where the wavefunction overlaps produce destructive interference in $\langle 0|\hat{n}|1\rangle$ while keeping $\langle 0|\hat{n}|2\rangle$ and $\langle 1|\hat{n}|2\rangle$ sizable and similar. Coupling rate under capacitive coupling to the transmission line is given by[7]:

$$\Gamma_{ij}^{\mathrm{ext}} \propto |\omega_{ij}|\, |\langle i|n|j\rangle|^2 \left| \coth\left(\frac{\hbar\omega_{ij}}{2k_B T}\right) + 1 \right| \tag{4.1}$$

Therefore, we can theoretically calculate for our levels of interest $\langle i|n|j\rangle$ using the parameters we got from fitting and determine at which point we can engineer a lambda system.

4.4.2 Experiments to locate Λ point

In our experiments, we aimed to identify the flux bias point that realizes a Λ configuration in the fluxonium spectrum. Ideally, this would be a point which we located in Fig. 4.13 at $\Phi/\Phi_0 = 0.48$. However, from our transition measurements (see Fig. 4.6), the $0 \leftrightarrow 2$ transition disappears before reaching the ideal Λ point. Therefore, we

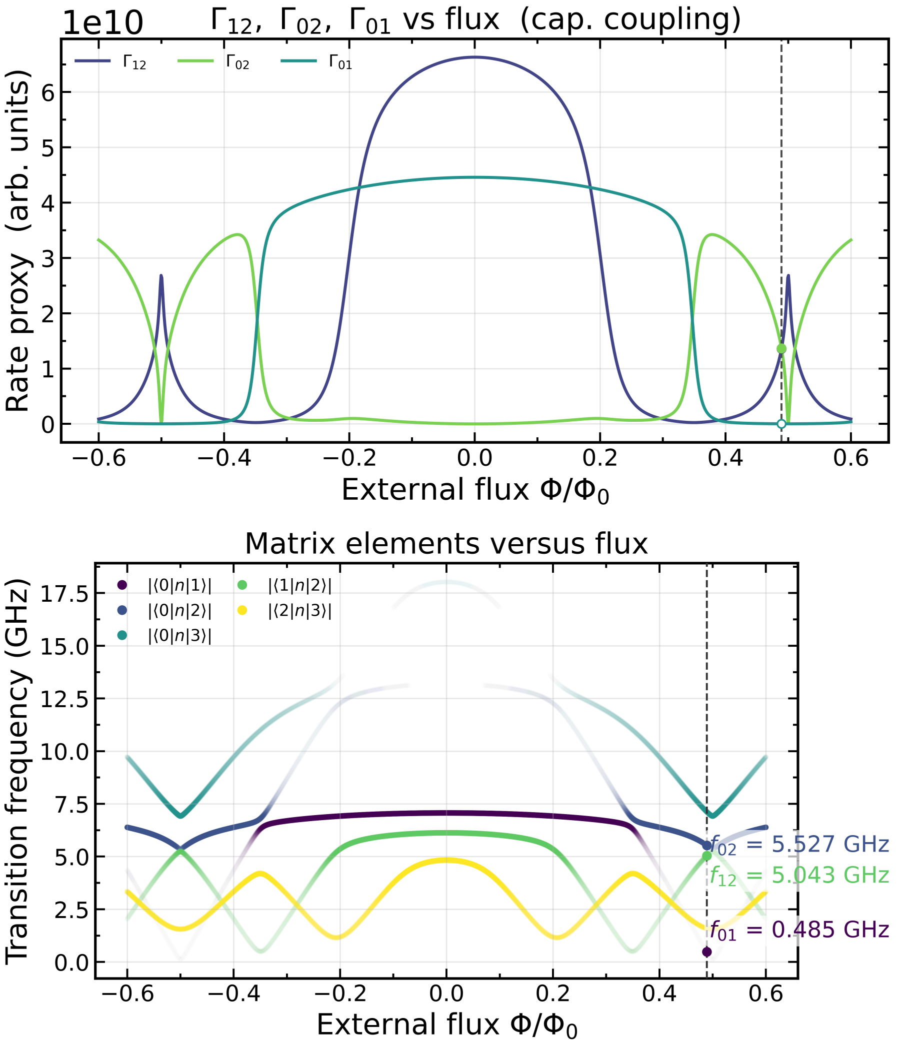

Figure 4.13: Plot of Γ_{ij} from Eq. (4.1) **in arbitrary units (top) and transition frequencies normalized to charge matrix elements (bottom)** | In the bottom plot, the color intensity of each point encodes the magnitude of the corresponding matrix element $|\langle i|n|j\rangle|$, normalized to its maximum value, with darker points indicating larger values. We locate the flux point where Γ_{02} and Γ_{12} are similar and sizable while Γ_{01} is low, which corresponds to external flux $\Phi/\Phi_0 = 0.48$. Dashed line in both plots this flux point.

first bias to a point close to this region and first map all observable transitions. As we already know that the $0 \leftrightarrow 1$ matrix element is intrinsically small, experimentally it is easier to locate the $0 \leftrightarrow 2$ transition first. Once $0 \leftrightarrow 2$ is identified, the $1 \leftrightarrow 2$ transition is found using a two-tone method: instead of pumping $0 \leftrightarrow 1$ and sweeping $1 \leftrightarrow 2$, we fix the VNA tone on the $0 \leftrightarrow 2$ frequency and sweep a pump tone. When the pump matches the $1 \leftrightarrow 2$ transition frequency, a peak appears in the response, arising from stimulated emission from $|2\rangle$ to $|1\rangle$.

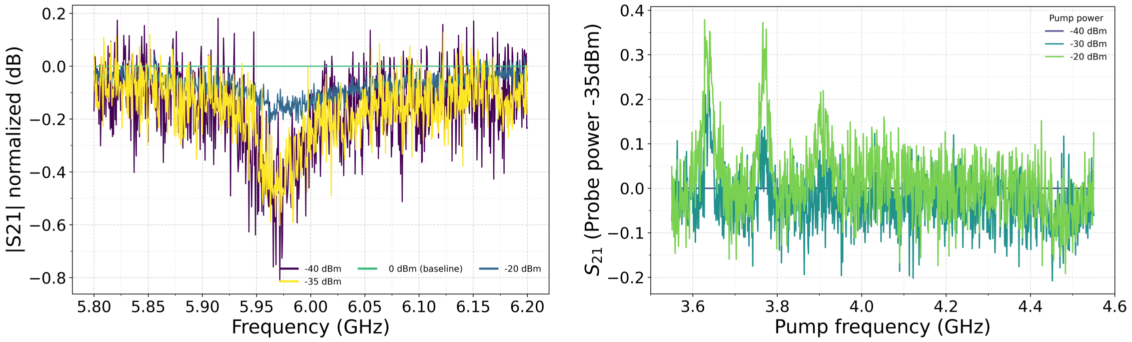

Figure 4.14: Power-dependent transmission $|S_{21}|$ versus frequency for the waveguide fluxonium device showing $0 \leftrightarrow 2$ transition (left) and power-dependent 2 tone measurement to locate $1 \leftrightarrow 2$ transition (right) | The measurements are done at flux biasing point of $\Phi/\Phi_0 = 0.45$, which are slightly away from desired Λ system flux bias point.

As shown in Fig. 4.14, the left panel identifies the $0 \leftrightarrow 2$ transition, from which we select an optimal probe power of $-35\,\text{dBm}$. The right panel displays three peaks in the S_{21} response near the expected $1 \leftrightarrow 2$ pump frequency, whereas a single peak is anticipated. The origin of this multiplicity is under investigation.

5

Conclusion

This thesis investigated fluxonium devices coupled either to a coplanar-waveguide (CPW) resonator or directly to a semi-infinite 50 Ω waveguide. We developed a complete workflow including design, electromagnetic and flux-bias simulation, cryogenic measurements and data analysis—that links design choices to measurable decay channels in multi-level dynamics.

For design, 3D EM simulation and energy-participation-ratio quantization provided circuit parameters that were consistent with the targeted operating regime, while magnetostatic simulations yielded a practical current-to-flux calibration for on-chip biasing. Fabrication produced working fluxonium devices in both the resonator-coupled and waveguide-coupled topologies, which is a great success for the design of JJ arrays. In the lab, we characterized the bare resonator, verified dispersive coupling where appropriate, and mapped the flux-dependent transition spectrum of the waveguide-coupled device. Using reflection measurements and a fit function derived from input–output theory, we extracted coupling parameters of the fluxonium and quantified the radiative and non-radiative contributions to decay.

The main takeaway is that the one-dimensional electromagnetic environment can be used as an engineered bath that selectively enhances or suppresses specific transitions in a multilevel atom. This is particularly interesting, as the physical system is very simple, comprising just an atom coupled to the waveguide, compared to other dissipation engineered systems.

In particular, we identified flux region in which matrix-element selection rules suppress the $0 \leftrightarrow 1$ transition while having sizable and similar rates on $0 \leftrightarrow 2$ and $1 \leftrightarrow 2$. This validates the central premise of the work: by designing circuit parameters of fluxonium artificial atom and also the electromagnetic profile of the environment, one can steer dissipation pathways toward systems such as Λ-type control.

Overall, we describe fabrication-reproducible design, simulation and quantitative spectroscopy and demonstrate that fluxonium in a planar environment is a viable platform for controlled dissipation and level-selective engineering.

Building on these results, our next step is to build and operate a Λ system using fluxonium eigenstates. On the device side, adjustments of E_j, E_c and E_L will help to position both $0 \leftrightarrow 2$ and $1 \leftrightarrow 2$ in a more easily accessible flux bias point. Successful demonstration of a fluxonium Λ-system would enable high-contrast fluorescence readout and controlled heat flows relevant to quantum thermodynamics experiments. Also, we will prototype a new device; the direct coupling with waveguide will still be maintained, while also including a planar readout resonator. This would allow for weak, quantum non-demolition (QND) readout outside the 4-8 GHz range, which is the current limitation.

A

Appendix 1

A.1 COMSOL workflow for flux-bias calibration

Our goal is to find the amount of current needed to thread exactly $\Phi_0/2$ through the fluxonium loop formed by JJ and JJ array. The calculation is performed with the `Magnetic Fields (mf)` interface in COMSOL MULTIPHYSICS® [40]. The key steps are summarised below.

The GDS file generated by Qiskit Metal is imported to the comsol file, so that the simulation catches the physics of the device. A Work Plane is used to create the 2-D shapes by 150 nm, matching the thickness of the aluminium film (Fig. A.1). To mimic the free space around the chip, a 600 μm sphere is created which encloses the device. Later this shpere will be assigned vacuum properties.

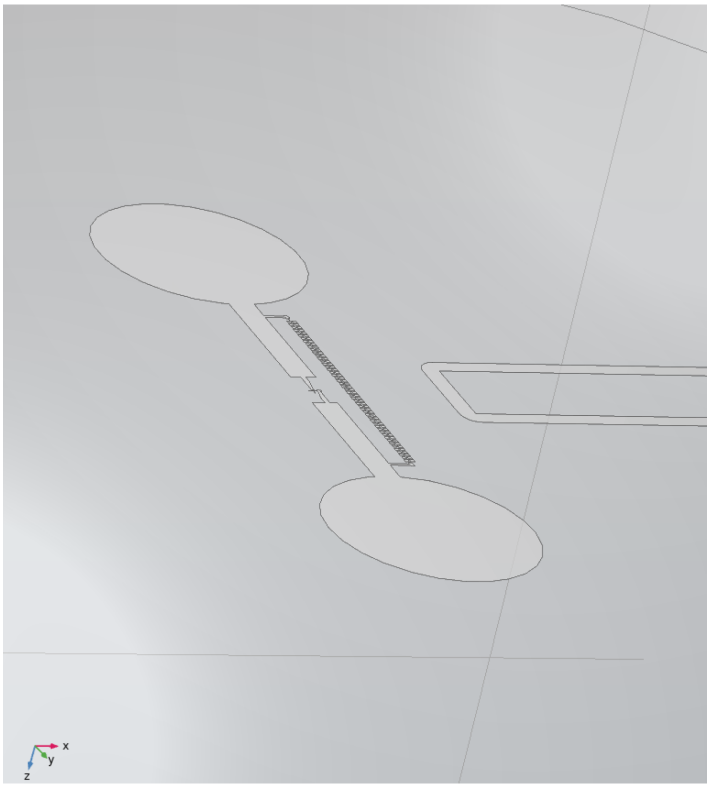

Figure A.1: Imported GDS layout extruded to 150 nm (grey) and enclosed in an air sphere. The bias line is shorted to the ground with one and and with other is connected to the port.

For simulation only two materials are required:

- **Air/vacuum** : default settings of $\varepsilon_r = 1,\ \mu_r = 1,\ \sigma = 0$.
- **Superconductor (Al)** : modelled as an impedance boundary with $\sigma = 10^7\,\mathrm{S/m},\ \mu_r = 10^{-4},\ \varepsilon_r = 1$. We use these values because we know that superconductor is an ideal conductor that is a diamagnet, it expels magnetic fields[41]. These finite extrema are the largest (smallest) values COMSOL accepts and approximate a perfect diamagnetic conductor.

We define the flux line as a coil domain and excite it with a reference current $I_0 = 1\,\mathrm{mA}$. To capture the full physics of a superconductor, we also take in the account Surface Current Density that is given by London Equation : $\mathbf{J}_s = -\lambda_L^{-2}\mathbf{A}_t$ and is imposed on the aluminium surface.

A two-step study solves first the coil geometry analysis and then a stationary magnetic problem.

Using the `Multislice` plot in logarithmic scale we visualise the magnetic-flux density and streamlines (Fig. A.2). The flux through the superconducting loop is obtained from

$$\Phi = \int_S \mathbf{B}\cdot d\mathbf{S} \;=\; \oint_{\partial S} \mathbf{A}\cdot d\mathbf{l},$$

where we used Stokes' theorem $\int_S (\nabla\times\mathbf{A})\cdot d\mathbf{S} = \oint_{\partial S} \mathbf{A}\cdot d\mathbf{l}$ and the relation $\mathbf{B} = \nabla\times\mathbf{A}$. As a contour whe chose a contour that encloses the loop

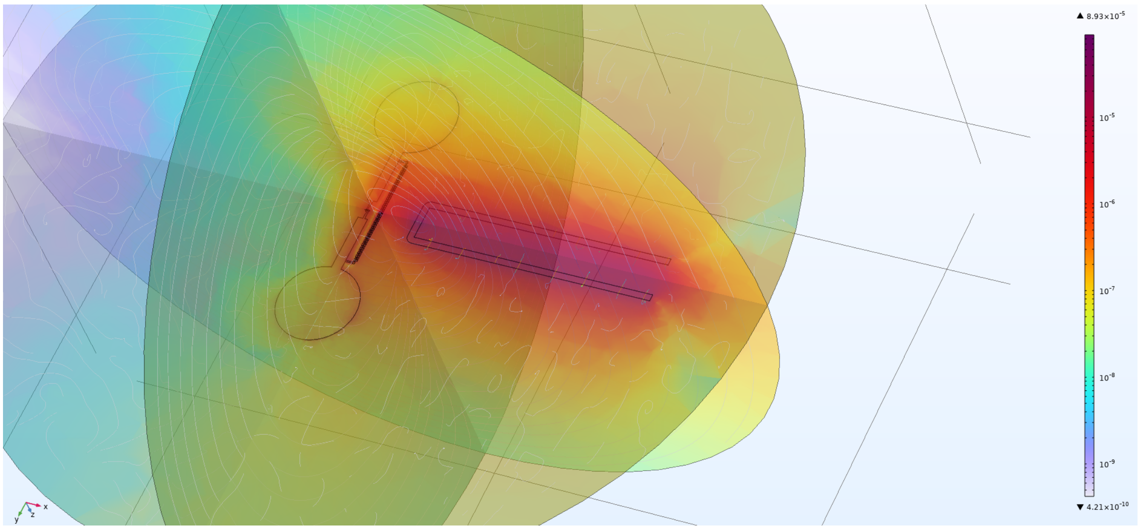

Figure A.2: Magnitude of the magnetic flux density (colour) and stream lines for a 1 mA bias current. The flux is concentrated through the loop because the surrounding superconductor repels the field.

The results suggest that the required current to thread a half flux quantum is

$$I_{1/2\Phi_0} \approx 2.7\,\mu\mathrm{A}.$$

Bibliography

[1] Mahdi Naghiloo. Introduction to experimental quantum measurement with superconducting qubits, 2019.

[2] P. Krantz, M. Kjaergaard, F. Yan, T. P. Orlando, S. Gustavsson, and W. D. Oliver. A quantum engineer's guide to superconducting qubits. *Applied Physics Reviews*, 6(2):021318, 2019.

[3] Michael A. Nielsen and Isaac L. Chuang. *Quantum Computation and Quantum Information: 10th Anniversary Edition.* Cambridge University Press, 2010.

[4] J. F. Poyatos, J. I. Cirac, and P. Zoller. Quantum reservoir engineering with laser cooling of trapped ions. *Physical Review Letters*, 77(23):4728–4731, 1996.

[5] A. Aamir, M. P. Jamet Suria, A. Marín Guzmán, J. C. Castillo-Moreno, M. Epstein, J. N. Yunger Halpern, and S. Gasparinetti. Thermally driven quantum refrigerator autonomously resets a superconducting qubit. *Nature Physics*, 21:318–323, 2025.

[6] Zaki Leghtas, S. Touzard, I. M. Pop, A. Kou, B. Vlastakis, A. Petrenko, K. M. Sliwa, A. Narla, S. Shankar, M. J. Hatridge, M. Reagor, L. Frunzio, R. J. Schoelkopf, M. Mirrahimi, and M. H. Devoret. Confining the state of light to a quantum manifold by engineered two-photon loss. *Science*, 347(6224):853–857, 2015.

[7] Shu Watanabe, Kotaro Hida, Kohei Matsuura, and Yasunobu Nakamura. Nondemolition fluorescence readout and high-fidelity unconditional reset of a fluxonium qubit via dissipation engineering. *Physical Review A*, 112(1):012624, 2025. Published 28 July 2025.

[8] Alexandre Blais, Ren-Shou Huang, Andreas Wallraff, Steven M. Girvin, and Robert J. Schoelkopf. Cavity quantum electrodynamics for superconducting electrical circuits: An architecture for quantum computation. *Physical Review A*, 69(6):062320, 2004.

[9] Serge Haroche and Jean-Michel Raimond. *Exploring the Quantum: Atoms, Cavities and Photons.* Oxford University Press, Oxford, UK, 2006.

[10] Andreas Wallraff, David I. Schuster, Alexandre Blais, Luigi Frunzio, Ren-Shou Huang, Johannes Majer, S. Kumar, Steven M. Girvin, and Robert J. Schoelkopf. Strong coupling of a single photon to a superconducting qubit using circuit quantum electrodynamics. *Nature*, 431(7005):162–167, 2004.

[11] Alexandre Blais, Arne L. Grimsmo, S. M. Girvin, and Andreas Wallraff. Circuit quantum electrodynamics. *Rev. Mod. Phys.*, 93:025005, May 2021.

[12] Massachusetts Institute of Technology (MIT) OpenCourseWare. 6.002 – Circuits and Electronics (Spring 2007). `https://ocw.mit.edu/courses/`

`6-002-circuits-and-electronics-spring-2007/`, 2007. Accessed: 19 May 2025.

[13] L. D. Landau and E. M. Lifshitz. *Mechanics*, volume 1 of *Course of Theoretical Physics*. Butterworth–Heinemann, Oxford, UK, 3rd edition, 1976.

[14] Y. Kitaev, A.˙Introduction of the term "superinductance". unpublished.

[15] Jens Koch, Terri M. Yu, Jay Gambetta, A. A. Houck, D. I. Schuster, J. Majer, Alexandre Blais, M. H. Devoret, S. M. Girvin, and R. J. Schoelkopf. Charge-insensitive qubit design derived from the cooper pair box. *Phys. Rev. A*, 76:042319, Oct 2007.

[16] U. Vool and M. H. Devoret. Introduction to quantum electromagnetic circuits. *Int. J. Circ. Theor. Appl.*, 2017. arXiv:1610.03438.

[17] C. Kittel. *Introduction to Solid State Physics*. Wiley, 5th edition, 1976.

[18] M. Tinkham. *Introduction to Superconductivity*. Dover, 2nd edition, 2004.

[19] Steven M. Girvin. Circuit qed: Superconducting qubits coupled to microwave photons. `https://boulderschool.yale.edu/sites/default/files/files/Girvin_CQED_LES_HOUCHES.pdf`, 2014. Les Houches Summer School Lecture Notes.

[20] B. D. Josephson. Possible new effects in superconductive tunnelling. *Physics Letters*, 1(7):251–253, 1962.

[21] Chang-Pin Wen. Coplanar waveguide: A surface strip transmission line suitable for non-reciprocal gyromagnetic device applications. *IEEE Transactions on Microwave Theory and Techniques*, 17(12):1087–1090, 1969.

[22] Rainee N. Simons. *Coplanar Waveguide Circuits, Components, and Systems*. Artech House, Boston, MA, 2004.

[23] V. E. Manucharyan, J. Koch, L. I. Glazman, and M. H. Devoret. Fluxonium: Single cooper-pair circuit free of charge offsets. *Science*, 326:113–116, 2009.

[24] N. A. Masluk, I. M. Pop, A. Kamal, Z. K. Minev, and M. H. Devoret. Microwave characterization of Josephson-junction arrays: Implementing a low-loss superinductance. *Physical Review Letters*, 109:137002, 2012.

[25] L.B. Nguyen, Y.-H. Lin, A. Somoroff, R. Mencia, N. Grabon, and V.E. Manucharyan. High-coherence fluxonium qubit. *Phys. Rev. X*, 9:041041, 2019.

[26] Long Bao Nguyen. *Toward the Fluxonium Quantum Processor*. Ph.D. dissertation, University of Maryland, College Park, 2020. Accessed 27 Jun 2025.

[27] U. Vool, A. Kou, W. C. Smith, N. E. Frattini, K. Serniak, P. Reinhold, I. M. Pop, S. Shankar, L. Frunzio, S. M. Girvin, and M. H. Devoret. Driving forbidden transitions in the fluxonium artificial atom. *Phys. Rev. Appl.*, 9:054046, May 2018.

[28] Vladimir Eduardovich Manucharyan. *Superinductance*. Ph.d. thesis, Yale University, New Haven, CT, 2012. Available online (accessed July 2025).

[29] D. Niepce, J. Burnett, and J. Bylander. High kinetic inductance nbn nanowire superinductors. *Physical Review Applied*, 14:034055, 2020.

[30] Alexandre Blais, Arne L. Grimsmo, Steven M. Girvin, and Andreas Wallraff. Circuit quantum electrodynamics. *Reviews of Modern Physics*, 93:025005, 2021.

[31] Kazuki Koshino and Yasunobu Nakamura. Control of the radiative level shift and linewidth of a superconducting artificial atom through a variable boundary condition. *New Journal of Physics*, 14(4):043005, 2012.

[32] Dennis Wang, Priti Shah, Marco Facchini, John Blair, Jeremy Drysdale, Thomas McConkey, and Zlatko Minev. A framework for quantum device design—project Qiskit Metal. In *APS March Meeting 2021, Session J30: Circuit Theory, Hamiltonian Analysis and Design ToolsI*, Virtual (Central Daylight Time, USA), 2021. American Physical Society. Abstract J30.00011, 5:24–5:36 PM.

[33] Florent Lecocq, Ioan M. Pop, Zhihui Peng, Iulian Matei, Thierry Crozes, Thierry Fournier, Cécile Naud, Wiebke Guichard, and Olivier Buisson. Junction fabrication by shadow evaporation without a suspended bridge. *Nanotechnology*, 22(31):315302, 2011.

[34] Zlatko K. Minev, Zaki Leghtas, Sourav O. Mundhada, Brian J. Lester, Steven Touzard, Kevin S. Chou, Won Son Paik, Brian Vlastakis, Sergey E. Nigg, Yvonne Chu, Andrew W. Cross, and Jerry M. Chow. Energy–participation quantization of Josephson circuits. *npj Quantum Information*, 7:131, 2021. Received 22 Oct2020; accepted 17 Jun2021; published 25 Aug2021.

[35] Guanyu Zhu, David G. Ferguson, Vladimir E. Manucharyan, and Jens Koch. Circuit qed with fluxonium qubits: Theory of the dispersive regime. *Phys. Rev. B*, 87:024510, Jan 2013.

[36] Figen Yilmaz, Siddharth Singh, Martijn F. S. Zwanenburg, Jinlun Hu, Taryn V. Stefanski, and Christian Kraglund Andersen. Energy–participation ratio analysis for very anharmonic superconducting circuits. *arXiv preprint*, November 2024.

[37] Bluefors. How does a dilution refrigerator work? `https://bluefors.com/stories/how-does-a-dilution-refrigerator-work/`, 2023. Accessed 9 Aug 2025.

[38] Sebastian Krinner, Simon Storz, Philipp Kurpiers, Paul Magnard, Johannes Heinsoo, Raphael Keller, Janis Luetolf, Christopher Eichler, and Andreas Wallraff. Engineering cryogenic setups for 100-qubit scale superconducting circuit systems. *EPJ Quantum Technology*, 6(2), 2019.

[39] S. Probst, F. B. Song, P. A. Bushev, A. V. Ustinov, and M. Weides. Efficient and robust analysis of complex scattering data under noise in microwave resonators. *Review of Scientific Instruments*, 86:024706, 2015.

[40] COMSOL AB. *COMSOL Multiphysics® User Guide*, 2024. Version 6.2.

[41] Fritz London and Heinz London. The electromagnetic equations of the supraconductor. *Proceedings of the Royal Society A*, 149(866):71–88, 1935.

DEPARTMENT OF SOME SUBJECT OR TECHNOLOGY
CHALMERS UNIVERSITY OF TECHNOLOGY
Gothenburg, Sweden
www.chalmers.se

CHALMERS
UNIVERSITY OF TECHNOLOGY